

2018

## PHYSICAL CHARACTERIZATION OF WARBURG EFFECT IN CANCER CELLS

Da Wei

University of Rhode Island, da\_wei@uri.edu

Follow this and additional works at: [https://digitalcommons.uri.edu/oa\\_diss](https://digitalcommons.uri.edu/oa_diss)

Terms of Use

All rights reserved under copyright.

---

### Recommended Citation

Wei, Da, "PHYSICAL CHARACTERIZATION OF WARBURG EFFECT IN CANCER CELLS" (2018). *Open Access Dissertations*. Paper 759.

[https://digitalcommons.uri.edu/oa\\_diss/759](https://digitalcommons.uri.edu/oa_diss/759)

This Dissertation is brought to you by the University of Rhode Island. It has been accepted for inclusion in Open Access Dissertations by an authorized administrator of DigitalCommons@URI. For more information, please contact [digitalcommons-group@uri.edu](mailto:digitalcommons-group@uri.edu). For permission to reuse copyrighted content, contact the author directly.

PHYSICAL CHARACTERIZATION OF WARBURG EFFECT IN CANCER CELLS

BY

DA WEI

A DISSERTATION SUBMITTED IN PARTIAL FULFILLMENT OF THE  
REQUIREMENTS FOR THE DEGREE OF  
DOCTOR OF PHILOSOPHY  
IN  
PHYSICS

UNIVERSITY OF RHODE ISLAND

2018

DOCTOR OF PHILOSOPHY DISSERTATION

OF

DA WEI

APPROVED:

Dissertation Committee:

Major Professor

Oleg A. Andreev

Yana K. Reshetnyak

Ying Sun

Jie Shen

DEAN OF THE GRADUATE SCHOOL

UNIVERSITY OF RHODE ISLAND

2018

## **ABSTRACT**

Cancer is the second leading cause of death in the United States after heart disease. Because the frequency of cancer diagnoses is correlated with life expectancy, we can expect the rate of cancer diagnosis to increase with the increase of life expectancy. Additionally, cancer treatments are notoriously costly and challenging due to the heterogeneity of the cancer cell population. For these reasons, devising methods to study the characteristics, efficiently diagnose and treat cancer is extremely important.

Warburg effect has been considered as the most unique mechanism that differ cancer cells from normal cells. Normally, most of the healthy cells predominantly produce energy by a low rate of glycolysis and oxidation of pyruvate in mitochondria, called oxidative phosphorylation. In the 1920s, Otto Warburg observed that tumors uptake a massive amount of glucose compared to its surrounding healthy tissues. Additionally, glycolysis was continued even in the presence of oxygen, called aerobic glycolysis. Cancer cells trend to metabolize excessive uptake of glucose and ferment to lactate unlike normal cells, even in the presence of oxygen and fully functioning mitochondria. This high rate of aerobic glycolysis in cancer cells is known as Warburg effect, which has been studied extensively especially after 2000s. Cancer cells have an unusually high rate of glycolysis and subsequently lactic acid fermentation to produce energy for cell activities, even under aerobic conditions, a seemingly inefficient way of producing energy.

It is recognized that cancer tumors undergo acidification due to the Warburg effect and

the overexpression of carbonic anhydrase enzymes at the surfaces of cancer cells, making acidity a universal tumor characteristic, and following the micro calories exchange during glycolytic fermentation. The more invasive the cancer is, the greater the extra-cellular acidosis and heat production.

The pH (Low) Insertion Peptides comprise a novel class of pH-sensitive targeting agents that spontaneously insert into cell membranes under acidic conditions. Therefore, the applicability of pHLIP® peptides to tumor-targeting applications is an obvious choice for investigation, it could be reconstructed with many different types of imaging and therapeutic agents. The membrane associated folding mechanism of action of pHLIP is triggered by low pH. The high concentration of proton in the low pH environment increase the protonation of the protonatable residues in pHLIP, which increase the overall hydrophobicity and drives the peptide into the hydrophobic core of the membrane, where it forms transmembrane helix. The two terminus of the peptide, one stays in the extracellular space while the other one pass through the membrane and locates into the cytoplasm.

With the creation of SNARF-pHLIP® construct in this work, it will allow me to measure the extra-cellular pH at the surface on the membrane of individual cancer cells. This will provide an advantage over measuring the bulk extra-cellular pH since it will result in higher contrast between normal, metastatic and non-metastatic cells, furthermore this novel construct could help with cancer diagnosing. I will apply it to metastatic and non-metastatic cancer cell lines. This will showcase that non-metastatic and metastatic cells can be distinguished from each other quickly and easily by their individual surface pHs.

Enhanced permeability and retention (EPR) effect is how most of the approved nanomedicinal products work though for cancer imaging and therapy. However, the heterogenous of cancers made them impossible to universally target. Extracellular acidity has been identified as a common property of cancerous cells, hence we can apply pHLIP® as a novel agent to coat noisome, making it has a high uptake near cancer cells.

## ACKNOWLEDGMENTS

I am very grateful to my advisor, Dr. Oleg A. Andreev, for his guidance: the amount of time and energy that he spent working with me over the past five years is enormous and I am sure that were it not for him, my graduate career would have ended much earlier and much less propitiously. The amount of time and care that Dr. Andreev dedicates to his graduate students is truly awesome and it amazes me that, given the amount of time that he dedicates to guiding his advisees, he is still such a productive member of the Physics Department, both in research and in managing the department as the dean. Aside from being grateful to him for constantly guiding me and motivating me when I needed it most, I am very happy to have been able to share interesting and enjoyable conversations with Dr. Andreev, and for his very pleasant sense of humor—an exception in physics much more than it is the rule. This sense of humor is shared with Dr. Yana K. Reshetnyak, another outstanding mentor who I feel privileged to have been able to work with. Conversations with Dr. Reshetnyak have always been enlightening, productive, and enjoyable, and I have never ceased being amazed by her seemingly endless knowledge.

I am indebted to Dr. Anna Moshnikova, who spent a great amount of her time teaching me lab techniques and experimental techniques, repeatedly explaining various chemical reactions to me, and running experiments with me. Interacting with Anna is always pleasant, and I am very grateful for her patience with me over the last five years. Without Anna, I would have spent a very long time looking for answers in the wrong locations. I am also very grateful to Dr. Dhammika Weerakkody, who spent a good deal of time

teaching me how to run and analyze biophysical experiments, and to the rest of the Division of Biological and Medical Physics for interesting and fruitful conversations.

I would like to thank Dr. Ying Sun and Dr. Jie Shen for serving on my graduate committee, particularly for the time they spent working with me and for fruitful and pleasant conversations over the course of my comprehensive and dissertation processes.

I owe a great deal of thanks to the faculty of the Physics Department of the University of Rhode Island, who have taught and guided me through undergraduate and graduate school. In particular, I am very grateful to Dr. Leonard M. Kahn and Dr. Alexander Meyerovich for helping and advising me through my graduate program. I am thankful to Dr. Gerhard Müller for dedicating a lot of time and energy to teaching many different fields of physics in an engaging and enjoyable manner (and for being an extremely entertaining, kind, and pleasant person), to Steve Pellegrino for many enjoyable conversations and for helping with my teaching responsibilities so much, and to Linda Connell for being so pleasant and helpful, and for working hard to make the department a much nicer and friendlier place.

Finally, I owe an enormous amount of thanks and gratitude to my family for their endless support and guidance, especially to my parents and my wife Cathleen

## PREFACE

This dissertation is written in “Manuscript” format, using the Thesis/Dissertation template of the University of Rhode Island. There are three manuscripts included in this dissertation, each of which comprises a chapter. The tables and figures of each manuscript are listed under the corresponding chapter in the list of tables and figures.

The results of our studies presented in the last chapters were published in the following papers:

1. Pereira MC, Pianella M, **Wei D**, Moshnikova A, Marianecchi C, Carafa M, Andreev OA & Reshetnyak YK. “pH-sensitive pHLIP® coated niosomes.” (2017) *Mol Membr Biol*. doi:10.1080/09687688.2017.1342969.

The first chapter is composed of research that has been submitted for publication in *Molecular Imaging and Biology*:

3. **Wei D**, Engelman DM, Reshetnyak YK and Andreev OA “Mapping of Acidity at Cancer Cells Surfaces.” *Manuscript submitted for publication*.

We are still working on collecting data and analysis for the second chapter, the results are in the hypothesis direction, it will be continued and published in the future.

## TABLE OF CONTENTS

<b>ABSTRACT</b> .....	ii
<b>ACKNOWLEDGMENTS</b> .....	v
<b>PREFACE</b> .....	vii
<b>TABLE OF CONTENTS</b> .....	viii
<b>LIST OF TABLES</b> .....	ix
<b>LIST OF FIGURES</b> .....	x
<b>CHAPTER 1</b> .....	1
pH Mapping at Cancer Cells Surface .....	1
<b>CHAPTER 2</b> .....	18
Measuring the Heat Production of Cancer Cells .....	18
<b>CHAPTER 3</b> .....	39
pH-sensitive pHLIP® coated niosomes.....	39

## LIST OF TABLES

### CHAPTER 1

There are no tables in Chapter 1.

### CHAPTER 2

There are no tables in Chapter 1.

### CHAPTER 3

Table 1. The mean hydrodynamic diameter, the zeta potential and the polydispersity index of niosomes in HEPES buffer at pH 7.4 ..... 66

Table S1. Organs uptake of niosomes at different time period..... 76

Table S2. Uptake of different niosomes in organs after 24 hours I.V. administration  
..... 77

## LIST OF FIGURES

### CHAPTER 1

Figure 1. Image analysis and outputs .....	14
Figure 2. Calibration curve and measured surface pH for the cell lines .....	16
Figure 3. Single M4A4 cell imaging and pH map .....	17

### CHAPTER 2

Figure 1. Heat production from HeLa cells detected by ITC.....	33
Figure 2. Optical system polarization .....	34
Figure 3. Fluorescent image of fluorescein as correction to the system .....	35
Figure 4. Processed HeLa-GFP image for anisotropy calculation.....	36
Figure 5. Image analysis and outputs .....	37
Figure 6. HeLa-GFP anisotropy result .....	38

### CHAPTER 3

Figure 1. TEM image and fluorescence spectra of niosomes .....	67
Figure 2. Cellular uptake of niosomes at low and high pH.....	68
Figure 3. Uptake and cellular distribution of niosomes by A549 lung cancer cells	69
Figure 4. Time-dependent distribution of niosomes uptake in organs.....	71
Figure 5. Rhodamine fluorescence images and mean surface fluorescence of organs after I.V. administration of pHLIP and PEG coated niosomes .....	72
Figure 6. Distribution of R18 fluorescent signal in tumor sections obtained at 24 hours compared with H&E stain.....	73

Figure S1. The SELDI-TOF mass spectrum of Pyr-pHLIP.....	78
Figure S2. The size histograms of the DSPE-pHLIP and Pyr-pHLIP containing niosomes.....	79
Figure S3. The stability study of DSPE-pHLIP and Pyr-pHLIP coated niosomes in buffer within 30 days .....	80
Figure S4. Fluorescent uptake of niosomes at low and high pH before and after treated with Trypan blue .....	81
Figure S5. Uptake and cellular distribution of niosomes by 4T1 lung cancer cells....	82

## CHAPTER 1

*Manuscript submitted for publication in Molecular Imaging & Biology*

### **pH Mapping at Cancer Cells Surface**

Da Wei<sup>1</sup>, Donald M. Engelman<sup>2</sup>, Yana K. Reshetnyak<sup>1</sup> and Oleg A. Andreev<sup>1</sup>

<sup>1</sup>Physics Department, University of Rhode Island, 2 Lippitt Rd., Kingston, RI 02874

<sup>2</sup>Department of Molecular Biophysics and Biochemistry, Yale, New Haven, CT 06511

Keywords: pHLIP, tumor acidity, pH measurements, SNARF fluorescence, tumor spheroids

## **ABSTRACT**

Solid tumors have an acidic extracellular environment, which results from the elevated glycolytic activity of cancer cells. Cancer cells maintain neutral intracellular pH (7.2) by transporting out protons and lactate acid. Acidity of extracellular microenvironment in tumor, and particularly near the cancer cells surface, is high. To validate this assumption, we recently introduced a novel approach of extracellular pH measurements at the surface of cells by using a pH-sensitive fluorescent dye, SNARF, conjugated to a pH Low Insertion Peptide (pHLIP® peptide), which targets plasma membranes of cells in acidic diseased tissue. Our original approach was based on measurements of fluorescence spectra of SNARF pHLIP. Here we present a novel pH mapping method, which allows measurements of pH of individual cells with high spatial resolution. Novel approach is based on the analysis of two fluorescent images of SNARF pHLIP formed by dual view optical system where one image is recorded using  $579\pm 17$  nm filter and other image using  $647\pm 28.5$  nm filter. We developed program to align images, find ratios between images and convert ratios into pH map for individual cells. An average pH for each cell and a pH histogram for all cells within the image are calculated. The data obtained on several cancer cell lines grown in spheroids indicate that in absence of glucose or in presence of deoxyglucose (non-metabolizable glucose analog) the pH at the surface of most cells were similar and close to the pH of bulk solution. While in presence of glucose highly metastatic cancer cells have lower surface pH than non-metastatic cells, and both cells types showed surface pH to be lower than bulk extracellular pH.

## INTRODUCTION

Otto Warburg discovered that cancer cells predominately use glycolysis for ATP production even when oxygen supply is sufficient, and he also found that tumor microenvironment is more acidic than that in normal tissues [1]. For many years the main tool of measuring pH in tumor tissue was a needle pH meter, which is an invasive method that damage cells and could not distinguish between intercellular and extracellular pHs [2]. It was believed that intracellular pHi and extracellular pHe were both acidic until it was shown that pHi is rather neutral (7.2) in both normal and cancer cells, while pHe is an acidic in tumors in contrast to normal pHe found in healthy tissue [3-5]. Tumor acidosis is caused mostly by the enhancement of glycolytic metabolism and an inhibition of phosphorylation-oxidation pathway of energy production [6, 7]. To maintain normal pHi cancer cells have to pump out protons produced during glycolysis [8]. Membrane carbonic anhydrases are inducing further cell surface acidification by hydrating cell-generated CO<sub>2</sub> into HCO<sub>3</sub><sup>-</sup> and H<sup>+</sup> at the cancer cell membrane [7]. As a result, it is expected that an “acidic layer” will be formed around cancer cells, and steep proton concentration gradient might exist near the surface of cancer cells. Thus, the cancer cells surface pH is the best measure of tumor acidity.

We recently introduced novel approach for cell surface pH measurements using pH Low Insertion Peptide (pHLIP) conjugated with pH sensitive ratiometric fluorescent dye, SNARF [9]. pHLIPs can target tumors and deliver imaging and therapeutic agents to cancer cells within tumors [10-15]. pHLIPs form transmembrane helix with N-terminus pointed outside a cell and C-terminus inserted across membrane. SNARF was conjugated to the N-terminus of pHLIP to measure pH near the surface of cancer cells

in extracellular space [9]. We used spectroscopic method to record SNARF emission at 580 nm and 640 nm, calculate ratio and convert it into pH values. However, this approach does not allow measuring of pH at a single cell level. Therefore, here we present a new pH mapping method to measure pH of individual cells with high spatial resolution.

## **MATERIALS AND METHODS**

### ***Materials***

D-(+)-glucose  $\geq 99.5\%$  and 2-deoxy-D-glucose  $\geq 99\%$  were purchased from Sigma-Aldrich. Matrigel® growth factor reduced basement membrane matrix, phenol red-free was obtained from Corning. The wild type (WT) pH (Low) Insertion Peptide, WT-pHLIP, was synthesized with a single Lys residue near its acetylated N-terminus (Ac-AKEQNPIYWARYADWLFTTPLLALLVDADEGT) and purified by reverse-phase chromatography at the C.S.Bio. SNARF™-1 carboxylic acid, acetate, succinimidyl ester was purchased from ThermoFisher Scientific.

### ***Phosphate-Buffered Solutions***

Phosphate-buffered solutions were prepared to obtain the pH range of 6.0-8.0 by mixing 0.5 M dibasic and monobasic solutions (J. T. Baker). The final experimental PBS solution contained 10 mM phosphate, 150 mM NaCl (J. T. Baker), 0.2 mM MgCl<sub>2</sub> (Sigma), and 0.2 mM CaCl<sub>2</sub> (Sigma). Buffer solutions were sterilized by passage through a 0.2- $\mu$ m filter. The final pH for each solution was measured by dual star pH / ISE benchtop meter with a microelectrode (Thermo Scientific™ Orion™).

### ***Synthesis of SNARF-pHLIP***

Lys-WT and SNARF-1 were dissolved in DMF (dimethylformamide, Sigma), and incubated at a ratio of 2:1 in 60% DMF (dimethylformamide), 30% 0.1 M PBS pH 9.0 and 10% pH 9.5 0.1 M sodium bicarbonate buffer for a final pH of 9.0. SNARF-1 was converted to its fluorescent form after conjugation by raising the conjugation solution's volume by 50% with methanol and raising the solution pH to 14 with 2 M potassium hydroxide for 1 hour. Then, pH was adjusted to pH 7.0 by adding 30% HCl. The reaction progress was monitored by reverse phase (Zorbax SB-C18 columns, 9.4 × 250 mm 5 μm, Agilent Technology) high-performance liquid chromatography (HPLC) using a gradient of 25–75% acetonitrile and water containing 0.05% of trifluoroacetic acid. The concentration of each labeled peptide in buffer was determined by SNARF-1 absorption at 548 nm,  $\epsilon_{548}=27,000 \text{ M}^{-1} \text{ cm}^{-1}$ . The purity and characterization of the construct was performed by analytical HPLC and surface-enhanced laser desorption/ionization–TOF mass spectrometry.

### ***Cell Lines***

Human melanoma M4A4 and NM2C5 cell lines were obtained from the American Tissue and Culture Collection (ATCC). Cells were authenticated, stored according to supplier's instructions, and used within 3–4 months after frozen aliquots resuscitations. All lines were cultured in Dulbecco's modified Eagle medium (DMEM) containing 4.5 g/L glucose and 40 mg/L sodium pyruvate supplemented with 10% FBS (Gibco), 0.1% of 10 μg/mL ciprofloxacin·HCl (Cellgro, Voigt Global Distribution) in a humidified atmosphere of 5% CO<sub>2</sub> at 37 °C.

### ***Tumor Spheroids***

A 2% agarose (Sigma) solution was made by dissolving in pH 7.4 PBS (Gibco). 150  $\mu$ L of the solution was pipetted into each well of a 48-well flat bottom tissue culture plate (Celltreat). After the agarose gel had sufficiently settled ( $\sim$ 1 h), 150  $\mu$ L of DMEM supplemented with 10% FBS and ciprofloxacin·HCl was added to each well. The covered plate was left in a humidified atmosphere at 37°C and 5% CO<sub>2</sub> in cell culture incubator for 24 h. Next day, the excess media was removed from the agarose layer. NM2C5 or M4A4 cells, 10,000 cells, in 200  $\mu$ L of DMEM contains 2% matrigel (Corning) were added into each well and kept in cell culture incubator for 3-4 days to allow formation of spheroids. Matrigel was dissolved on ice overnight and added in ice cold DMEM at a concentration of 2.5% (to obtain final 2% once added to the wells). Then the mixture was heated to 37°C before being combined with cells.

### ***Imaging Tumor Spheroids***

Tumor spheroids of a given cell line were incubated in 50  $\mu$ L of PBS buffer, pH6.3 containing 5  $\mu$ M SNARF-pHLIP and either 25 mM glucose or 50 mM deoxyglucose in a humidified atmosphere of 5% CO<sub>2</sub> at 37°C for 30 min. After treatment the spheroids were washed three times in 1 mL of experimental PBS of the desired pH containing either 25 mM glucose or 50 mM deoxy-glucose for control. Next, the spheroids were placed into a 96 wells glass bottom dish for imaging.

The fluorescence images were recorded using Olympus IX71, an inverted epifluorescence microscope, using FF01-531/40-25 Semrock excitation filter; a DV2 multichannel imaging system, with FF01-579/34-25 and FF01-647/57-25 Semrock

emission filters in left and right channels, respectively, which allowed two images to be taken at the same time by Q-imaging Retiga-SRV CCD.

### ***Data Analysis***

For each pH point, 20 spheroids were used in total: 10 spheroids were used for calibration, and 10 spheroids were used for cancer cell surface pH measurements. For calibration and pH measurements glucose and deoxy-glucose were added to 5 spheroids, respectively. 5 images were taken from different spots of each spheroid. All images were analyzed by our program written in Matlab R2016b. The output of analysis included a correction curve, pH map and pH histogram for the selected cells in each image. Statistical analysis and final graphs were obtained using Origin Lab 2016.

## **RESULTS**

To measure pH at the surface of cancer cells we used pHLIP conjugated with pH sensitive fluorescent dye, SNARF, at the N-terminus of the peptide, which stays exposed to the extracellular space after insertion into plasma membrane of cancer cells. Previously we demonstrated using quenching of SNARF fluorescence by membrane impermeable Trypan Blue that SNARF pHLIP is not taken by endocytosis, and SNARF indeed is located in the extracellular space and reports about cell surface pH [9]. Fluorescence spectrum of SNARF exhibits two maxima at 580 nm and 640 nm, the ratio of intensities of which correlates with pH of microenvironment. The advantage of ratiometric method is that it does not depend on concentration of SNARF and allows to measure pH with high accuracy. The intensities of two emission maxima can be obtained from fluorescence spectrum recorded by linear CCD camera simultaneously in

the range of 570 - 700 nm, as it was done in our previous work [9]. The spectroscopic method is accurate, however, it measures only an average intensity values from the illuminated spot, which includes multiple cells and space between cells [9]. In this work we developed pH mapping approach. SNARF fluorescence was excited using  $531\pm 20$  nm excitation filter, and emission signal was split into two using DV2 optical system to acquire two fluorescent images, where one image was obtained using  $579\pm 17$  nm emission filter (called 580 nm) and the other image is obtained using  $647\pm 28.5$  nm emission filter (called 640 nm). Both images are originated from the same area and acquired simultaneously by the same CCD camera, which exclude any influence of potential intensity fluctuations on calculated pH values. The interface of image analysis program in Matlab is presented on Figure 1. First, correction at a pixel level is applied in order to align two selected regions from the image (Figure 1a). The intensity values of each pixel at the center (within the region of  $\pm 25$  pixel units) of the selected 640 nm image region are compared with the corresponding central pixels intensity values of 580 nm image region (Figure 1b). The differences in intensity between 640 nm and 580 nm images are shown in Figure 1f. Two images are adjusted to reach minimum of the intensity differences and align images for further processing. Intensity (Figure 1c) and size (Figure 1d) cutoff were used to establish cell border outline (red outlines in Figure 1e). The pH mapping is obtained by calculating the averaged intensity ratio for each cell and converting these ratios into pH values using calibration curves (Figure 1g). The pH histogram reflects distribution of the surface pH for all selected cells (Figure 1h).

The calibration curves were obtained for NM2C5 (Figure 2a) and M4A4 (Figure 2b) cancer cells separately. M4A4 or NM2C5 tumor spheroids were incubated in media with

no glucose and then transferred into media containing of 50 mM of non-metabolizable analog of glucose, deoxyglucose. The inhibition of glycolysis results in shutdown of acid production by cells, and flux of protons. As a result, the pH at the surface of cells became the same as in the bulk solution, which was used to calibrate fluorescence signal with pH. We recorded numerous cells images at different buffer pH and calculated 580/640 ratio images (RM4A4 and RNM2C5) to establish calibration curves for each cancer cell lines (Figure 2a, b):

for M4A4 cells:  $pH = (9.990 \pm 0.111) - (5.182 \pm 0.190) \cdot R_{M4A4}$

for NM2C5 cells:  $pH = (10.187 \pm 0.100) - (5.257 \pm 0.155) \cdot R_{NM2C5}$

The calibrations curves are slightly different for M4A4 and NM2C5 cells, which might be attributed to the difference in membrane protein and/or lipid compositions.

The calibration equations were used to calculate surface pH from the SNARF pHLIP 580/640 nm ratio imaging of non-metastatic cancer cell line, NM2C5, and metastatic cancer cell line, aM4A4, in the presence of 25 mM glucose, which promotes cellular metabolism. In the presence of glucose, both NM2C5 and M4A4 cells show lower pH at the surface compared with the bulk extracellular pH. Furthermore, metastatic cancer cells were slightly more acidic than non-metastatic cancer cells, especially when the pH of media was normal or higher than pH 7.4. When the pH of media is lower than pH 6.4, the pH at the surface of cancer cells equilibrates with bulk solution pH (Figure 2a, b). The surface pH differences (difference in pH found in the presence of glucose and deoxy-glucose) for each type of cancer cells are shown in Figure 2c. At normal or high

pH of media the metastatic cancer cells, M4A4, exhibit a significantly larger pH difference, about 0.7 pH units, compared to the non-metastatic cancer cells, NM2C5, pH difference of which is about 0.3 pH units (Figure 2d).

Finally, 100x magnification objective was used to image single M4A4 cells in tumor spheroids (Figure 3). Instead of calculating the average intensity for cell, we calculated the intensity ratios at each pixel inside a single cell to establish pH mapping. The obtained results clearly indicate that the surface pH within a single cell is not uniform, which might be associated with segregation of proton pumps.

## **DISCUSSION**

In early days tumor acidity was measured mostly by microelectrodes directly inserted into tumor tissue. It was demonstrated that tumors are acidic and it was believed at that time that extracellular and intracellular, pHe and pH<sub>i</sub>, were both acidic [4]. However, microelectrodes could not directly measure pH inside of a cell. Only after development of magnetic resonance spectroscopy (MRS) methods it was found that pH<sub>i</sub> in cancer cells is similar to or slightly more basic than that in normal cells, while pHe in tumors was more acidic than pHe in healthy tissues [3, 5]. MRS methods are using pH sensitive agents to measure pHe in tumors in vivo [16]. Those agents are distributed in both blood (where pH is normal) and extracellular space. Thus, MRS provides measure of an averaged pH in tumors [17-21]. Since cancer cells have to maintain pH<sub>i</sub> in the range of pH 7.2 – 7.4 for normal cellular functions, they have to pump out protons and lactate, which are produced in high amounts due to the enhancement of glycolysis [1]. The other by-product is CO<sub>2</sub>, which freely diffuses across membrane and is converted into

carbonic acid by membrane proteins, carbonic anhydrases (CAIX, CAXII), overexpressed in cancer cells [22-24]. Protons create high acidity zone near the cancer cell membrane. pH increases with distance from the cancer cells, and bulk extracellular pH might be normal in a well perfused tumor areas, or might remain low in a poorly perfused tumor zones. Despite on variations of bulk extracellular pH in tumors (documented by MRS measurements) cell surface pH is much more stable parameter, which correlates well with metastatic potential of cancer cells. Therefore, it is important to develop tools of cell surface pH measurements to investigate tumor development and progression. And, it is crucial for pH targeting approaches to sense acidity at the cell surface, as pH-LIP does, for targeting of imaging and therapeutic agents to all cancer cells within tumors. In this work we introduced new method to map cell surface pH at the level of individual cancer cells. We believe, the introduced approach can find many applications in cancer biology studies, and it might be translated to the clinics for pH measurements on tissue samples removed in the course of needle biopsy or surgery.

## REFERENCES

1. Warburg, O., *On the origin of cancer cells*. Science, 1956. **123**(3191): p. 309-14.
2. Griffiths, J.R., *Are cancer cells acidic?* Br J Cancer, 1991. **64**(3): p. 425-7.
3. Griffiths, J.R., et al., *<sup>31</sup>P-NMR investigation of solid tumours in the living rat*. Biosci Rep, 1981. **1**(4): p. 319-25.
4. Wike-Hooley, J.L., J. Haveman, and H.S. Reinhold, *The relevance of tumour pH to the treatment of malignant disease*. Radiother Oncol, 1984. **2**(4): p. 343-66.
5. Zhang, X., Y. Lin, and R.J. Gillies, *Tumor pH and its measurement*. J Nucl Med, 2010.

- 51**(8): p. 1167-70.
6. Kroemer, G. and J. Pouyssegur, *Tumor cell metabolism: cancer's Achilles' heel*. *Cancer Cell*, 2008. **13**(6): p. 472-82.
  7. Damaghi, M., J.W. Wojtkowiak, and R.J. Gillies, *pH sensing and regulation in cancer*. *Front Physiol*, 2013. **4**: p. 370.
  8. Chiche, J., M.C. Brahimi-Horn, and J. Pouyssegur, *Tumour hypoxia induces a metabolic shift causing acidosis: a common feature in cancer*. *J Cell Mol Med*, 2010. **14**(4): p. 771-94.
  9. Anderson, M., et al., *Probe for the measurement of cell surface pH in vivo and ex vivo*. *Proc Natl Acad Sci U S A*, 2016. **113**(29): p. 8177-81.
  10. Andreev, O.A., et al., *Mechanism and uses of a membrane peptide that targets tumors and other acidic tissues in vivo*. *Proc Natl Acad Sci U S A*, 2007. **104**(19): p. 7893-8.
  11. Andreev, O.A., D.M. Engelman, and Y.K. Reshetnyak, *pH-sensitive membrane peptides (pHLIPs) as a novel class of delivery agents*. *Mol Membr Biol*, 2010. **27**(7): p. 341-52.
  12. Reshetnyak, Y.K., et al., *Measuring tumor aggressiveness and targeting metastatic lesions with fluorescent pHLIP*. *Mol Imaging Biol*, 2011. **13**(6): p. 1146-56.
  13. Weerakkody, D., et al., *Family of pH (low) insertion peptides for tumor targeting*. *Proc Natl Acad Sci U S A*, 2013. **110**(15): p. 5834-9.
  14. Andreev, O.A., D.M. Engelman, and Y.K. Reshetnyak, *Targeting diseased tissues by pHLIP insertion at low cell surface pH*. *Front Physiol*, 2014. **5**: p. 97.
  15. Wyatt, L.C., et al., *Applications of pHLIP Technology for Cancer Imaging and Therapy: (Trends in Biotechnology 35, 653-664, 2017)*. *Trends Biotechnol*, 2017.
  16. Hashim, A.I., et al., *Imaging pH and metastasis*. *NMR Biomed*, 2011. **24**(6): p. 582-91.
  17. Moon, R.B. and J.H. Richards, *Determination of intracellular pH by <sup>31</sup>P magnetic*

- resonance*. J Biol Chem, 1973. **248**(20): p. 7276-8.
18. Gillies, R.J., Z. Liu, and Z. Bhujwala, *<sup>31</sup>P-MRS measurements of extracellular pH of tumors using 3-aminopropylphosphonate*. Am J Physiol, 1994. **267**(1 Pt 1): p. C195-203.
  19. Ojugo, A.S., et al., *Measurement of the extracellular pH of solid tumours in mice by magnetic resonance spectroscopy: a comparison of exogenous (<sup>19</sup>F) and (<sup>31</sup>P) probes*. NMR Biomed, 1999. **12**(8): p. 495-504.
  20. Garcia-Martin, M.L., et al., *Mapping extracellular pH in rat brain gliomas in vivo by <sup>1</sup>H magnetic resonance spectroscopic imaging: comparison with maps of metabolites*. Cancer Res, 2001. **61**(17): p. 6524-31.
  21. Rata, M., et al., *Comparison of three reference methods for the measurement of intracellular pH using <sup>31</sup>P MRS in healthy volunteers and patients with lymphoma*. NMR Biomed, 2014. **27**(2): p. 158-62.
  22. Wykoff, C.C., et al., *Hypoxia-inducible expression of tumor-associated carbonic anhydrases*. Cancer Res, 2000. **60**(24): p. 7075-83.
  23. Griffiths, J.R., et al., *Why are cancers acidic? A carrier-mediated diffusion model for H<sup>+</sup> transport in the interstitial fluid*. Novartis Found Symp, 2001. **240**: p. 46-62; discussion 62-7, 152-3.
  24. Ivanov, S., et al., *Expression of hypoxia-inducible cell-surface transmembrane carbonic anhydrases in human cancer*. Am J Pathol, 2001. **158**(3): p. 905-19.

## FIGURES

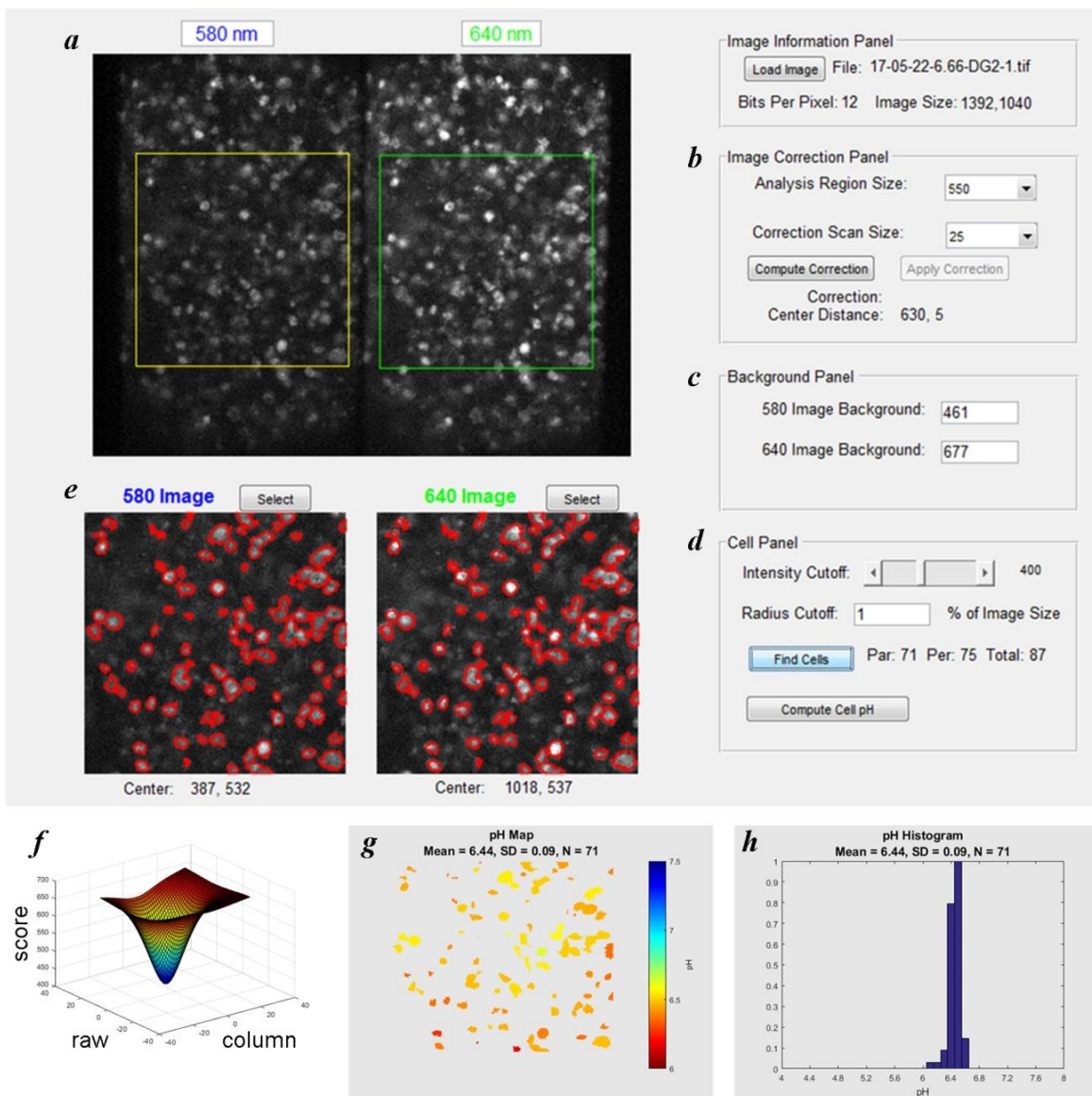


**Figure 1.** The interface of image analysis program in Matlab is shown. Fluorescence 580 nm and 640 nm images (*a*) were obtained using DV2 beam splitting system and  $579\pm 17$  nm and  $647\pm 28.5$  nm emission filters, respectively. The area of interest is selected by squares. Image correction (*b*), intensity (*c*) and size cutoff (*d*) panels of interface are presented, which are used to establish cell border outlines shown in red (*e*).

The differences in intensity values in each pixel at the center (within the region of  $\pm 25$  pixels) between 640 nm and 580 nm image regions (*f*) were used to adjust 580 nm image position to reach minimum of the intensity differences (achieve the smallest score) and align images for further processing. pH map (*g*), where pH values are indicated by different colors, and pH histogram (*h*) calculated for the selected region from (*a*).

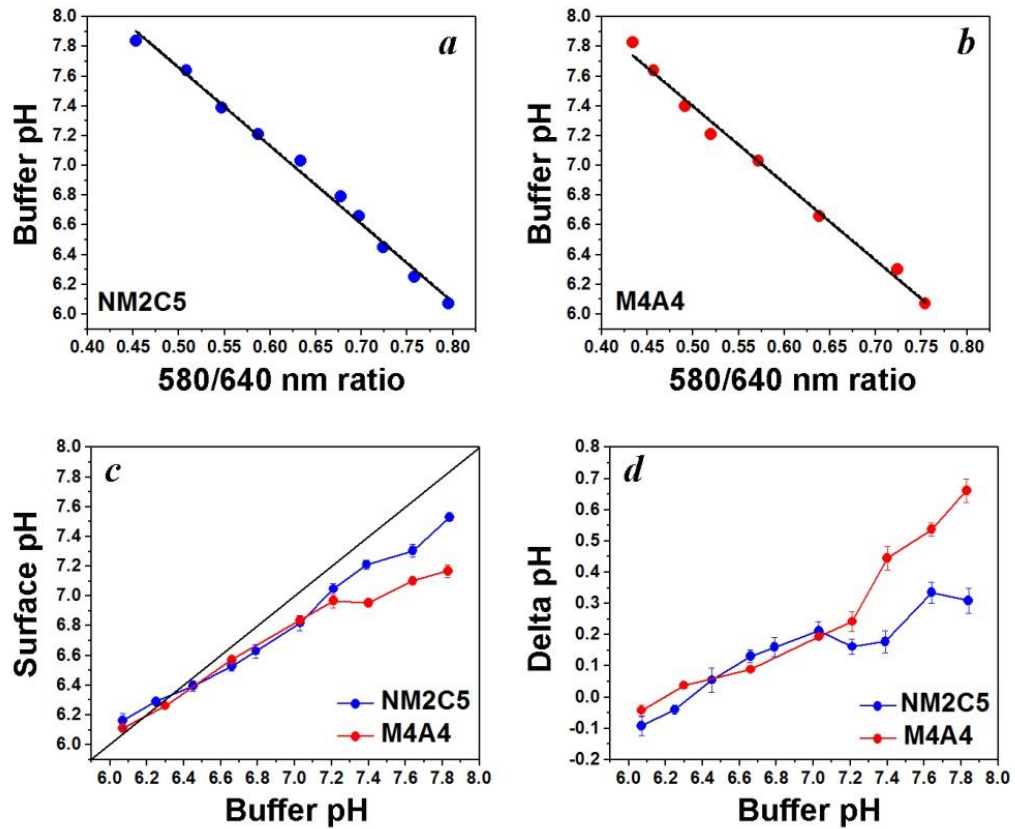


**Figure 2.** Calibration curves for NM2C5 (*a*) and M4A4 (*b*) cells grown in tumor spheroids obtained by linear fit of buffer pH vs 580/640 SNARF fluorescence intensity ratio in presence of 50 mM deoxy-glucose at various pHs of buffer. Cell surface pH (*c*) measured using SANRF pHLIP in NM2C5 and M4A4 cell spheroids in the presence of 25 mM glucose at various pHs of buffer were calculated using calibration curves (*a* and *b*) obtained for each cell line to convert 580/640 nm fluorescence ratios into pH values. The cell surface pH differences (*d*) for non-metastatic NM2C5 and metastatic M4A4 cancer cells were calculated by comparing pH values obtained in the presence of deoxy-glucose and glucose at different pHs of buffer.

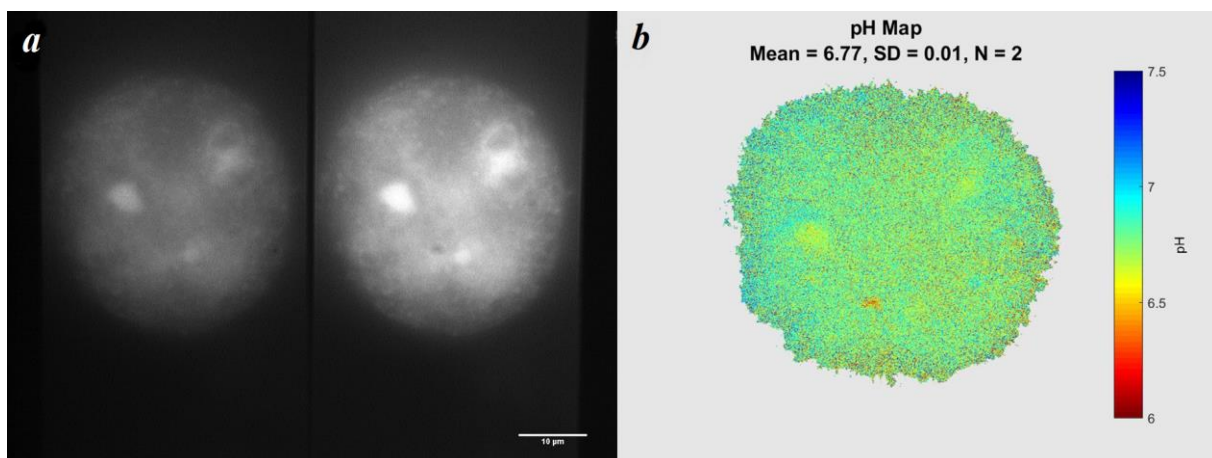


**Figure 3.** (a) Single cell was selected on the surface of M4A4 tumor spheroids and two images were acquired using DV2 system with 580 (left) and 640 (right) nm filters. (b) Left and right images were aligned and 580/640 nm intensities ratios were calculated for each pixel, the ratios were converted in pH values and presented as pH map with color scale shown on the right.

## **CHAPTER 2**

### *Collecting Data*

#### **Measuring the Heat Production of Cancer Cells**

Da Wei, Oleg A. Andreev and Yana K. Reshetnyak

Physics Department, University of Rhode Island, 2 Lippitt Rd., Kingston, RI 02874

Keywords: heat production, ITC, anisotropy, Hela-GPF, fluorescence imaging

## **Abstract**

Warburg effect has been considered as the most unique mechanism that differ cancer cells from normal cells. Normally, most of the healthy cells predominantly produce energy by a low rate of glycolysis and oxidation of pyruvate in mitochondria, called oxidative phosphorylation. In the 1920s, Otto Warburg observed that tumors uptake a massive amount of glucose compared to its surrounding healthy tissues. Additionally, glycolysis was continued even in the presence of oxygen, called aerobic glycolysis [1, 2]. Cancer cells trend to metabolize excessive uptake of glucose and ferment to lactate unlike normal cells, even in the presence of oxygen and fully functioning mitochondria. Cancer cells have an unusually high rate of glycolysis and subsequently lactic acid fermentation to produce energy for cell activities, even under aerobic conditions, a seemingly inefficient way of producing energy. This high rate of metabolism leads to the metabolic chemical reactions and ions directional flows in living cells driven by electrochemical potentials and energy-consuming pumping processes, which all together would result in the heat production. In this research, we designed experiments to measure heat production by cancer cells due to their metabolic activity. From the isothermal calorimetry measurements, we estimated that HeLa cells produce about 40 times more heat per second than regular Chinese Hamster Ovarian cell. From intracellular temperature measurements, we also observed that GFP – HeLa incubated with glucose has a higher temperature than incubated with deoxy-glucose.

## **Introduction**

The metabolic chemical reactions and the various kinds of ions directional flows in living cells driven by electrochemical potentials and energy-consuming pumping processes is hypothesized to result in the heat production [3, 4]. Steep temperature gradients in cells have attracted strong interest from cell biologists recently, especially concerning the effects of local intracellular thermogenesis on the rates of chemical reactions, the rate of the diffusion process, the speed of exocytosis [5], and so on. The peculiarities of energy metabolism in cancer cells are imputable not only to a markedly glycolytic phenotype, but also to some essential features, such as a heavy imbalance in the NADH/NAD<sup>+</sup> ratio with a marked increase of lactate and decrease of pyruvate production [6-8]. Temperature is of fundamental importance in many cellular processes such as cell metabolism, cell division and gene expression [5, 9, 10]. Accurate and noninvasive monitoring of temperature changes in individual cells could thus help clarify intricate cellular processes and develop new applications in biology and medicine.

In a long history of the physiological studies on thermogenesis, the thermodynamic parameters have mainly been examined for different parts of the body, tissues or organs, as a whole [5-8]. With the development of new methods and technologies, there are appeared some recent studies on thermogenesis at single-cell level. In this part, I will introduce the methods that we developed for single cell heat production measurements, progresses and some results.

## **Isothermal Titration Calorimeter (ITC) for extracellular heat production measurement**

ITC is a technique used in quantitative studies of a wide variety of biomolecular interactions. ITC is the only technique that can simultaneously determine all binding parameters in a single experiment. A complete thermodynamic profile of the molecular interaction, including binding constants ( $K_D$ ), reaction stoichiometry ( $n$ ), enthalpy ( $\Delta H$ ) and entropy ( $\Delta S$ ) could be accurately calculated by measuring the heat transfer during binding [11]. Not only given binding affinities, ITC is particularly useful as it elucidates the mechanisms underlying molecular interactions, which leads to further optimization of compounds and more confident decision making [12]. In our research, ITC was used to monitor the heat production by cancer cells after injection with glucose or deoxy-glucose.

ITC has been used to directly measure the heat production that is either released or absorbed during a biomolecular binding event. It is composed of two identical cells made of a highly efficient thermally conducting and chemically inert material such as Hastelloy alloy or gold, surrounded by an adiabatic jacket. One of the cells is called reference cell, which is usually filled with buffer or water; the other one is sample cell, where the reaction take place when injecting the second component to the sample. The microcalorimeter needs to keep these two cells at the same temperature. If there is a difference between two cells when binding occurs, the sensor can detect the difference in temperature and give feedback to the heaters, the heaters that making direct connection with the cells will start compensating until the temperature in the sample cell is the same with the reference cell. The heat exchange during the reaction, which is a

few millionths of a degree Celsius, will be detected and measured by the output of the heater to maintain the temperature balance.

In our ITC experiment, we loaded 5 million HeLa cells that have been starved in the medium without glucose overnight into measuring unit, then injected glucose or deoxy-glucose and monitored the heat exchange for 10 hours. All solutions in this experiment were degassed, since it is often necessary to obtain good measurements as the presence of gas bubbles within the sample cell will lead to abnormal data plots in the recorded results. The entire experiment took place under computer control. As described in Figure1, negative heat flow means the reaction is exothermic, the temperature in the sample cell increases upon addition of glucose, which lead to the decreases for the feedback power to the sample chamber to maintain an equal temperature between the two chambers. As the temperature of the two chambers reach equilibrium, the heat flow line reached a plateau. The first heat flow spike/pulse at 0 second gives the total heat released upon glucose or deoxy-glucose injections, and mixing process. It has been observed that a plateau was reached in 1 hour after injection of deoxy-glucose while after glucose injection it took about 4 hours. The heat release, which is the integral of the curve, also indicates that HeLa has more heat production with glucose injection than with deoxy-glucose that. We estimated that single HeLa cell generates about 4 nW, which is about 40 times higher than that for regular Chinese Hamster Ovarian cell (0.1 nW), and 13 times higher than human fibroblasts (0.3 nW).

## **Green Fluorescent Protein (GFP) Anisotropy for intracellular heat production measurement**

In physics, as opposed to isotropy, anisotropy means inhomogeneity in all directions. It is the quality of exhibiting properties being directional dependent, which implies different values when measured along axes in different directions. Anisotropy is most easily observed in regular lattices, in which atoms, ions, or molecules are arranged regularly. Usually these lattices include single crystals of solid elements or compounds [13]. In life science, fluorescence anisotropy, which is a population of fluorophores illuminated by a linearly polarized light that re-emits partially polarized fluorescence due to the random orientation of the molecular dipoles [14]. A strong light source is generally required for fluorescence polarization measurements. The light wave coming from this source can have an unlimited number of orientations. A polarization filter transmits only light of one orientation of electric vector. Fluorophore molecule can be considered as a linear oscillator, which would absorb light with a probability proportional to cosine of angle between dipole vector and electric vector of excitation light and it would emit light with probability of orientation of electric vector proportional to the cosine of angle between emitting dipole and electric vector of emitted light. Use another polarization filter for emission signal, the strength of the signal changes according to the orientation of the emitted light. The emitted light that has the same orientation as the polarized excitation filter completely passes the same orientation emission polarized filter. The emitted light that is perpendicular to the polarized excitation filter is completely blocked by the same filter. The anisotropy  $r$  of a light source is defined as the ratio of polarized components:

$$r = \frac{I_z - I_y}{I_x + I_y + I_z}$$

When we use two excitation polarization filters that have the perpendicular orientations, one is in the same orientation with the polarized excitation filter, another one is perpendicular to it, two polarized intensities that perpendicular to each other could be detected. If the excitation polarizer is in z-axis, then the parallel emission from fluorophore is symmetric in the same orientation, the perpendicular emission polarizer will be in xy- plan. Statistically, we have  $I_x = I_y$ , as  $I_y = I_{\perp}$ ,  $I_z = I_{\parallel}$ , the anisotropy of fluorophore has become:

$$r = \frac{I_{\parallel} - I_{\perp}}{I_{\parallel} + 2 I_{\perp}}$$

To calculate the fluorescence anisotropy, we just need to measure the polarized emission intensities that parallel and perpendicular to the polarized excitation light.

For immobilized randomly oriented dipoles anisotropy of emitted light could be 0.4 if emission and excitation dipoles are collinear, and -0.2 if they are perpendicular. Fluorophores in solution are very mobile and dipole can rotate during excited state and emit at different angle, which leads to depolarization of emitted light. Depolarization of fluorescence depends on ratio of rotational correlation time and fluorescence life time. Rotational correlation time decreases with increase of temperature while fluorescence life time is less sensitive to temperature. The fluorophores, which are molecular level particles that suspended in cytoplasm, have molecular rotation [15]. The measured value  $r$  is closely related to molecular rotation, according to Perrin's equation:

$$\frac{1}{r} = \frac{1}{r_0} \left(1 + \frac{\tau_F}{\tau_R}\right)$$

Where  $r_0$  is a constant called "limiting anisotropy",  $\tau_F$  is another constant called

fluorescence lifetime and  $\tau_R$  is rotational correlation time, while  $\tau_R$  depends on the temperature  $T$ , the viscosity  $\eta(T)$ , and the hydrodynamic volume  $V$ .  $\tau_F$  does not. According to Debye-Stoke-Einstein equation:

$$\tau_R = \frac{V \eta(T)}{k_B T}$$

Temperature could be measured by using fluorescence anisotropy. When the temperature increases, the molecular rotation of the fluorophores is accelerated, they move faster in a given amount of time. Faster movement means that the polarization of the light is conserved for a shorter time, which means that an increase in temperature results in lower polarization signal. Consequently, an increase in temperature leads to a decrease of the fluorescence polarization anisotropy. This technique has a lot of advantages compare to other methods, the ratiometric measurement is absolute intensities independent, common issues like photobleaching and fluorophore migration could be eliminated. This method is also noninvasive for cells, which provides more accurate and optimistic results.

In our previous study, we constructed optical system and developed the software to create and analyze the fluorescence anisotropy images of cells, single molecules and nanoparticles. The system includes the inverted microscope (Olympus IX71), two calcite prisms (CPs) inserted in the excitation and emission optical paths, and a CCD camera (Retiga-SRV, Q-imaging Co.). The excitation light was passed through the pinhole diaphragm, split by CP into two orthogonally polarized beams and focused by objective into two spots. The emission CP splits the fluorescence image of each spot into two images formed by horizontally and vertically polarized emission lights. The

CCD camera simultaneously records four images so the fluctuation in intensity of excitation light does not affect anisotropy values and, most importantly, that two polarized components corresponds exactly to the same state of a sample. We are using this system to study the “blinking” effect of quantum dots, binding of fluorescently labeled molecules to proteins, DNA, RNA in cells.

In this research, we used a new optical system that almost identical to the cell surface pH measurement. Instead of measuring the two excitation peaks from the fluorescent dye, SNARF, we are capturing the polarized fluorescent signals at two perpendicular directions from green fluorescent protein (GFP). The first direction is parallel to the incident polarized light’s direction, the second one is perpendicular to the incident polarization. GFP is one of the most widely studied and used proteins that extracted from jellyfish, which is a fluorophore that re-emits partially polarized fluorescence due to the random orientation of the molecular dipoles. We used GFP transfected HeLa in our experiments. Since GFP was expressed in the cytoplasm of HeLa cells, the temperature that measured in the experiment would be the local temperature of intracellular space. Temperature imaging technique for HeLa – GFP combines high spatial resolution and fast read-out with full biocompatibility.

In the optical system, a vertically polarized filter was installed between the microscope and the lamp, to turn the incident light into polarized light to the randomly oriented GFP inside of the cells, only those molecules that are oriented properly in the polarized plane can absorb light, become excited, and subsequently emit polarized light in a plane. On the side, the protein fluorescence signal goes into the beam splitter that contains a

vertical and a horizontal polarizer on each side, and split the incident beam into two identical beams for each side. One beam will pass through the vertically polarized filter, which is parallel to the incident light, the intensity is  $I_{\parallel}$ . The identical split beam will pass through the horizontal polarized filter, which is perpendicular to the incident light, this intensity is  $I_{\perp}$ . The signals were recorded by the CCD camera in the same image on the right and left side, as a result, the emitted light was measured in both the vertical and horizontal planes. To check the orientation of the polarizers, an external polarizer was used under bright field with a calibration slide, when the external polarizer was rotated, the intensities will change based on the angle between the polarizers. When the external polarizer rotates to the vertical orientation, the vertically signal will completely pass the filter, while the horizontally signal completely being blocked by the filter (Figure 2), indicating the polarizers are in the correct experimental orientation.

G factor is the instrument sensitivity ratio towards vertically and horizontally polarized light [16]. In fluorescence anisotropy measurements, the G factor is not related to properties of the sample but is purely an experimental correction for the polarization bias of the detection system. For accurate measurement, G factor has to be considered in the equation.

$$r = \frac{I_{\parallel} - G I_{\perp}}{I_{\parallel} + 2 G I_{\perp}}$$

G factor is also measured by exciting the sample using vertically polarized light and subsequently measuring the vertically and horizontally polarized components of the emission intensity, each for the same period of time. Since there is no difference between the numbers of photons coming towards the vertical and horizontal channels

from the sample, G factor is calculated as the ratio between the measured total intensities in each channel. For anisotropy imaging we need to do correction all image pixels. To calculate the G factor, fluorescein was used as correction sample. As the fluorescence anisotropy for fluorescein is close to zero due to the complete random orientation of the small molecule and very low rotational correlation time (<1 ns),  $i_{//}$  and  $i_{\perp}$  should be equals to each other theoretically, the intensity difference in the two orientations will be caused by the optical system. (Figure 3) By measuring  $i_{//}$  and  $i_{\perp}$ , G factor could be calculated by  $G = \frac{i_{//}}{i_{\perp}}$ .

To apply the detection system correction to the samples, the equation can be converted to:

$$r = \frac{I_{//} - G I_{\perp}}{I_{//} + 2 G I_{\perp}} = \frac{I_{//} - \frac{i_{//}}{i_{\perp}} I_{\perp}}{I_{//} + 2 \frac{i_{//}}{i_{\perp}} I_{\perp}} = \frac{\frac{I_{//}}{i_{//}} - \frac{I_{\perp}}{i_{\perp}}}{\frac{I_{//}}{i_{//}} + 2 \frac{I_{\perp}}{i_{\perp}}}$$

Thus, an image calculation for both sides of the image at the same time, cell image divided by fluorescein solution image would apply the G factor to the sample (Figure 4). Once the G factor has been applied to the cell image, the image can be processed by the further modified Matlab code for anisotropy imaging. The procedures are identical to pH imaging, including load the image, select sections from two sides of the image, apply the correction for the selected sections to align the regions, subtract the lowest intensity value in the regions as background to the cells, contour the cells based on intensity and area cutoff, calculate the fluorescence protein anisotropy for each contoured cell, plot anisotropy map and histogram for each image with all the selected

cells (Figure 5).

During the experiment, two dishes with 50,000 HeLa-GFP cells were grown in 300 $\mu$ L DMEM with high glucose in a collagen coated glass bottom microwell dish for one day, the medium was changed to DMEM without glucose to starve the cells overnight in the incubator, which is a humidified atmosphere of 5% CO<sub>2</sub> and 95% air at 37°C. On the third day, cells were washed three times with pH 7.4 PBS contains physiological level ions, then stayed in 300 $\mu$ L experimental PBS buffer contains 25mM glucose, and another dish with 50mM deoxy-glucose as comparison. After 30 minutes in room temperature to reach temperature equilibrium, the cells in the dishes were used for imaging. The fluorescence images were recorded through Olympus IX71, an inverted epifluorescence microscope, using a vertical polarization filter and GFP-3035B-OMF-ZERO Semrock filter set; a DV2 multichannel imaging system, with vertical polarized and horizontal polarized filter in left and right channels respectively, which allows images that have different information on the two sides taken at the same time by Qimaging Retiga-SRV CCD. Fluorescence images of the samples were taken by using Q-capture Pro 7. 10, images for each situation was taken and analyzed through Matlab 2016b. Statistic and result graphs were constructed by Origin Lab 2016.

In the result, anisotropy values were indicated in y axis (Figure 6). There is a clear difference of 0.00836 in anisotropy between samples incubated with glucose and deoxy-glucose. Cells incubated with glucose have a lower anisotropy, indicating that these cells have an overall higher temperature. The result is in agreement with what we have assumed from the beginning and the result we got from ITC experiment.

Since a higher temperature for cancer cells incubated with glucose has been confirmed, and the anisotropy difference is 0.00836. What are the temperatures for the cells in each case? To determine the temperature, a calibration experiment between measured anisotropy and local temperature around cells was performed. The same amount of HeLa-GFP were prepared in the same procedures, starved overnight in DMEM without glucose and incubated in 3mL PBS with same concentration of deoxy-glucose the next day, so it would be possible to measure the buffer temperature in the dish with EXTECH EsayView™ 10 thermometer. The temperature of the sample was controlled by Tokai Hit stage top incubator from 20°C to 40°C. Images were taken 20 minutes after the stage temperature have reached setting, the local temperature of cells were determined by the reading of thermometer for each image. After calculating the anisotropy value in each image at different temperatures, an equation of fluorescence protein anisotropy and cell temperature will be acquired. Thus, the cell temperature could be determined by knowing the anisotropy. The temperature was controlled from 22.5°C to 38.5°C, and the measured anisotropy was from 0.23 – 0.15, with a 0.08 anisotropy unit difference. An estimation of 1°C corresponds to 0.005 anisotropy unit, thus, the estimated temperature difference between cells incubated with glucose and deoxy-glucose is about 1.6°C.

## REFERENCES

1. Warburg, O., *Über den stoffwechsel der carcinomzelle*. Naturwissenschaften, 1924. **12**(50): p. 1131-1137.
2. Warburg, O., *Iron, the Oxygen-Carrier of Respiration-Ferment*. Science, 1925. **61**(1588):

- p. 575-82.
3. Chen, D.P., et al., *Hydrodynamic model of temperature change in open ionic channels*. Biophys J, 1995. **69**(6): p. 2304-22.
  4. Prigogine, I. and D. Kondepudi, *Modern thermodynamics. From heat engines to dissipative structures*, 1998.
  5. Andrews, Z.B., S. Diano, and T.L. Horvath, *Mitochondrial uncoupling proteins in the CNS: in support of function and survival*. Nat Rev Neurosci, 2005. **6**(11): p. 829-40.
  6. Patel, M.S. and L.G. Korotchkina, *Regulation of mammalian pyruvate dehydrogenase complex by phosphorylation: complexity of multiple phosphorylation sites and kinases*. Exp Mol Med, 2001. **33**(4): p. 191-7.
  7. Fantin, V.R., J. St-Pierre, and P. Leder, *Attenuation of LDH-A expression uncovers a link between glycolysis, mitochondrial physiology, and tumor maintenance*. Cancer cell, 2006. **9**(6): p. 425-434.
  8. Kim, J.W. and C.V. Dang, *Cancer's molecular sweet tooth and the Warburg effect*. Cancer Res, 2006. **66**(18): p. 8927-30.
  9. Lowell, B.B. and B.M. Spiegelman, *Towards a molecular understanding of adaptive thermogenesis*. Nature, 2000. **404**(6778): p. 652-60.
  10. Kamei, Y., et al., *Infrared laser-mediated gene induction in targeted single cells in vivo*. Nature methods, 2009. **6**(1): p. 79.
  11. Patel, M.S. and L.G. Korotchkina, *Regulation of mammalian pyruvate dehydrogenase complex by phosphorylation: complexity of multiple phosphorylation sites and kinases*. Experimental & molecular medicine, 2001. **33**(4): p. 191.
  12. Doyle, M.L., *Characterization of binding interactions by isothermal titration calorimetry*. Curr Opin Biotechnol, 1997. **8**(1): p. 31-5.

13. Schwertmann, U. and R.M. Cornell, *Iron oxides in the laboratory: preparation and characterization*. 2008: John Wiley & Sons.
14. Donner, J.S., et al., *Mapping intracellular temperature using green fluorescent protein*. Nano letters, 2012. **12**(4): p. 2107-2111.
15. Valeur, B. and M.N. Berberan-Santos, *Molecular fluorescence: principles and applications*. 2012: John Wiley & Sons.
16. Cehelnik, E., K. Mielenz, and R. Velapoldi, *Polarization effects on fluorescence measurements*. Journal of Research of the National Bureau of Standards-A. Physics and Chemistry, 1974. **79**.

## FIGURES

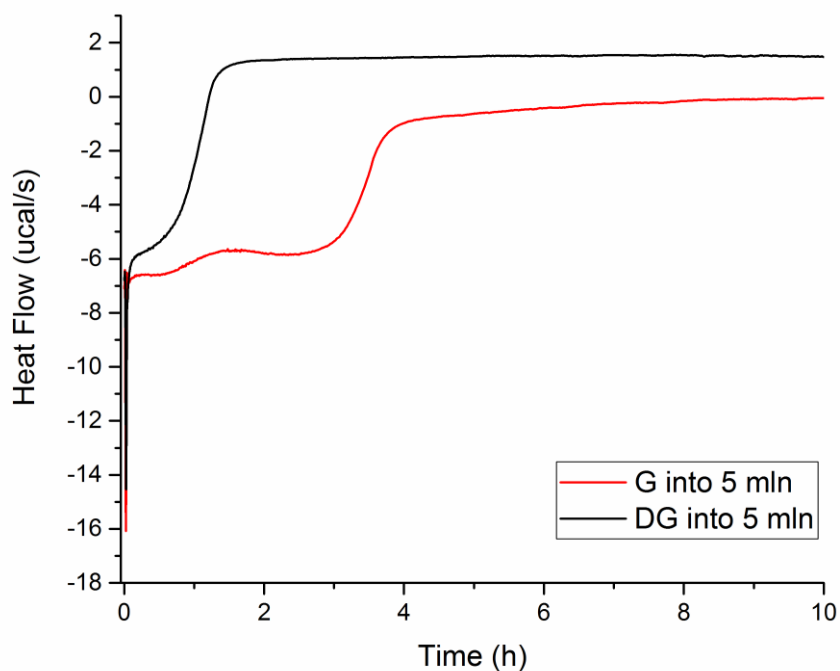


**Figure 1. Heat production from HeLa cells detected by ITC.** The first heat flow spike/pulse at 0 second gives the total heat exchanged in the glucose/deoxy-glucose injection, which is the heat released when mixing two liquids together. Deoxy-glucose injection takes about 1 hour to reach equilibrium and glucose injection takes about 4 hours. The heat release, which is the integral of the curve, indicating HeLa cells release more heat production with glucose injection.



**Figure 2. Optical system polarization.** When the external polarizer rotates to the vertical orientation, the vertically signal will completely pass the filter (right side), while the horizontally signal completely being blocked by the filter (left side).

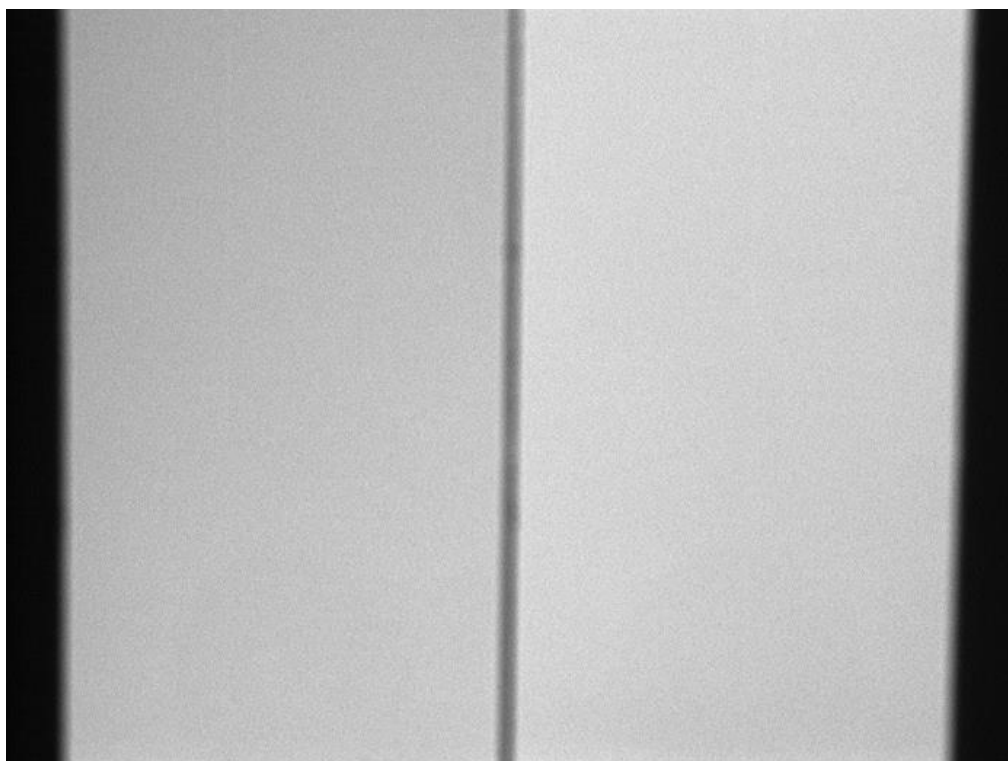


**Figure 3. Fluorescent image of fluorescein as correction to the system.** As the fluorescence protein anisotropy for fluorescein is zero due to the complete random orientation of the molecule. By applying this correction to the images, G factor and the uneven intensity distribution from lamp will be eliminated.

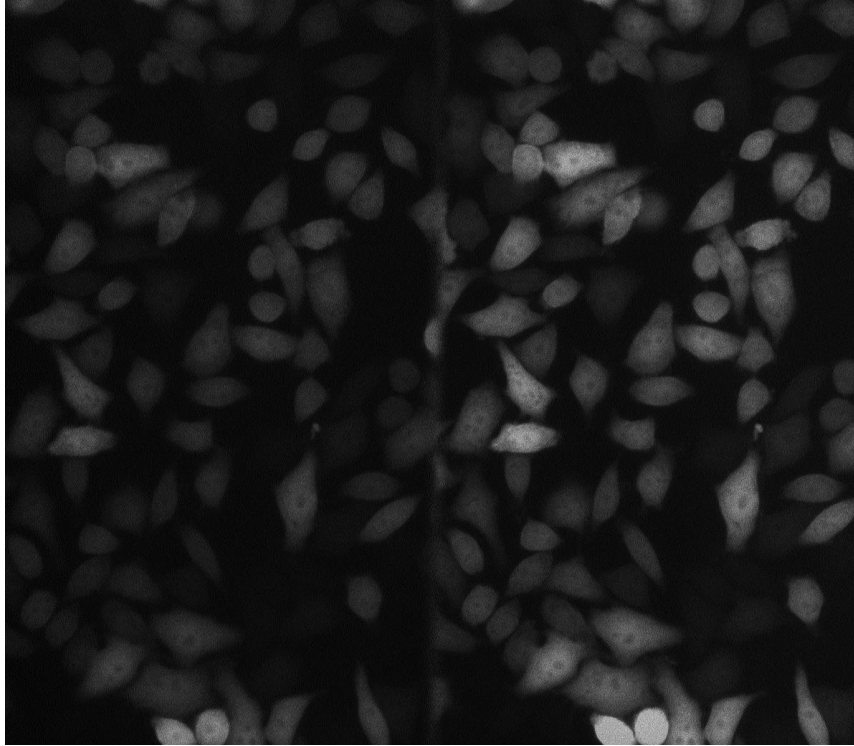


**Figure 4. Processed HeLa-GFP image for anisotropy calculation.** The original images were divided by the G factor image, and the black regions on the sides were cropped in ImageJ for better Matlab processing. Parallel intensity comes from the right side, and perpendicular intensity comes from the left side of the image.

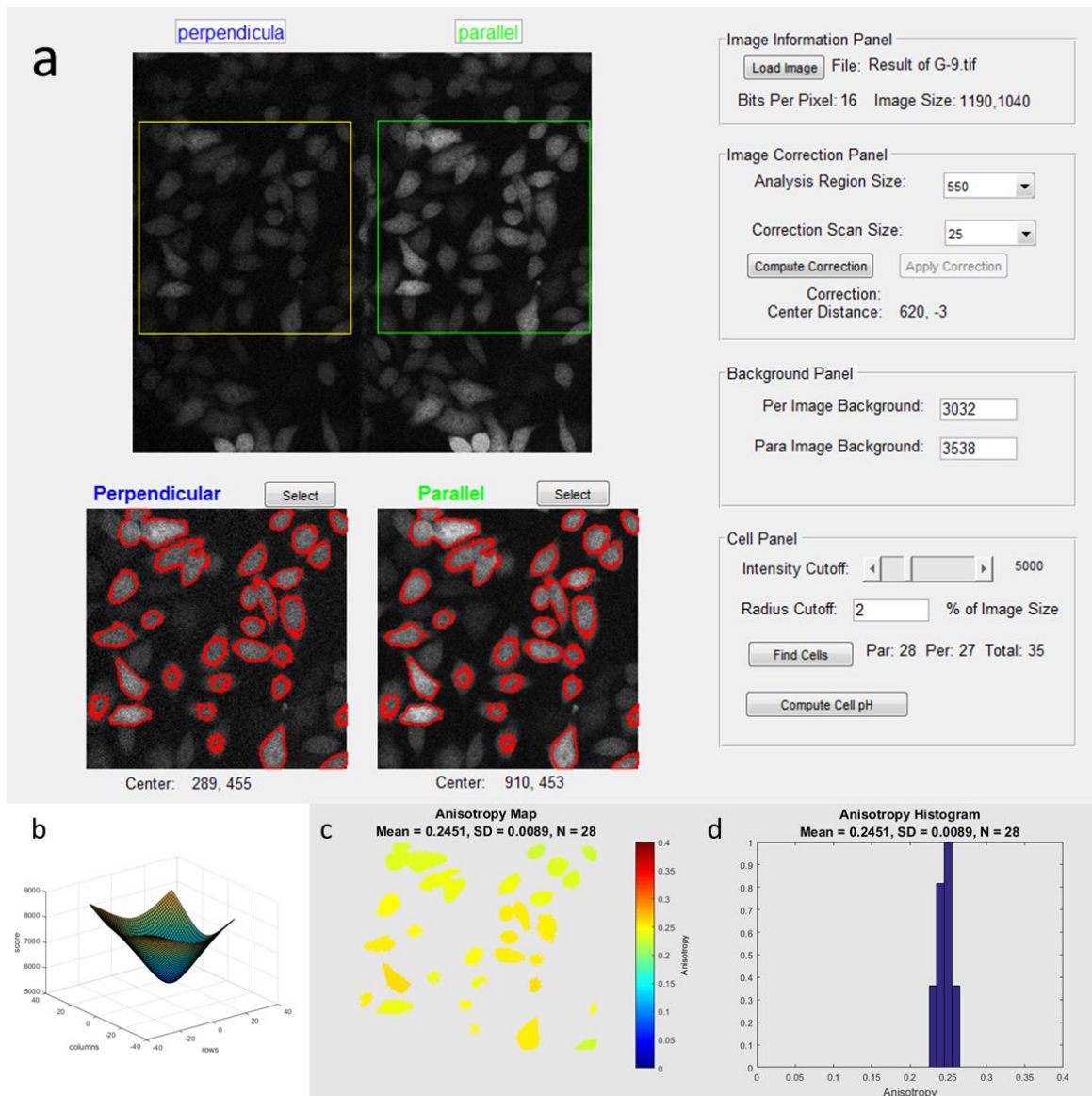


**Figure 5. Image analysis and outputs. a.** The interface of image analysis program created by Matlab. **b.** Differences in intensity value between the center of selected perpendicular region and  $\pm 25$  pixels units from the center of selected parallel region. The correction distance was applied to the selected parallel region by using the location of smallest score pixel. **c.** Anisotropy map for the selected cells in **a.**, anisotropy values are indicated by different colors for each cell. **d.** Anisotropy histogram for the selected cells in **a.**.

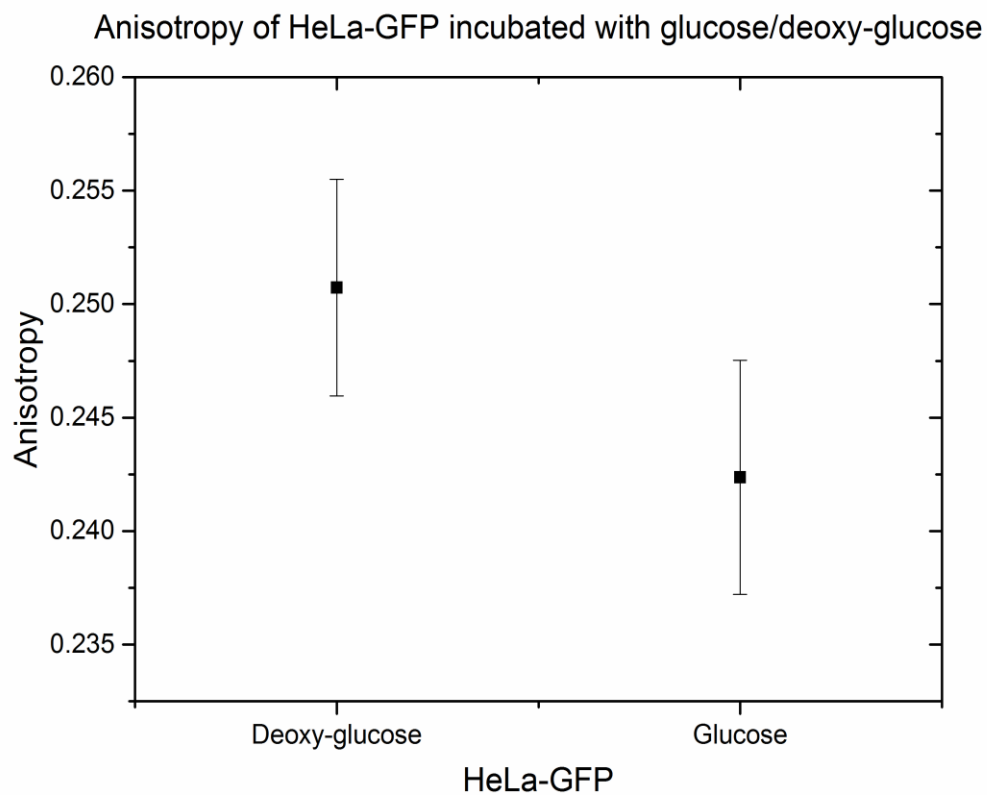


**Figure 6. HeLa-GFP anisotropy result.** The anisotropy for HeLa-GFP incubated with glucose has a lower value than incubated with deoxy-glucose, indicating that HeLa-GFP has a higher temperature with glucose incubation.

## CHAPTER 3

*Published in Molecular Membrane Biology in August 2017*

### **pH-sensitive pHLIP® Coated Niosomes**

Mohan C. Pereira<sup>1</sup>, Monica Pianella<sup>2</sup>, Da Wei<sup>1</sup>, Anna Moshnikova<sup>1</sup>,  
Carlotta Marianecchi<sup>2</sup>, Maria Carafa<sup>2</sup>, Oleg A. Andreev<sup>1</sup>, Yana K. Reshetnyak<sup>1</sup>

<sup>1</sup>Physics Department, University of Rhode Island, 2 Lippitt Rd., Kingston, RI  
02881, USA

<sup>2</sup>Dipartimento di Chimica e Tecnologie del Farmaco, Sapienza Università di  
Roma, P.zzle A. Moro 5 00185 Roma, Italia

Keywords: drug delivery, targeting tumor acidity, fluorescence imaging

## **Abstract**

Nanomedicine is becoming very popular over conventional methods due to the ability to tune physico-chemical properties of nanovectors, which are used for encapsulation of therapeutic and diagnostic agents. However, the success of nanomedicine primarily relies on how specifically and efficiently nanocarriers can target pathological sites to minimize undesirable side effects and enhance therapeutic efficacy. Here, we introduce a novel class of targeted nano drug delivery system, which can be used as an effective nano-theranostic for cancer. We formulated pH-sensitive niosomes (80-90 nm in diameter) using non-ionic surfactants Span20 (43-45 mol%), cholesterol (50 mol%) and 5 mol% of pH (Low) Insertion Peptide (pHLIP) conjugated with DSPE lipids (DSPE-pHLIP) or hydrophobic fluorescent dye, pyrene, (Pyr-pHLIP). pHLIP in coating of niosomes was used as an acidity sensitive targeting moiety. We have demonstrated that pHLIP coated niosomes sense the extracellular acidity of cancerous cells. Intravenous injection of fluorescently labeled (R18) pHLIP-coated niosomes into mice bearing tumors showed significant accumulation in tumors with minimal targeting of kidney, liver and muscles. Tumor-targeting niosomes coated with pHLIP exhibited 2-3 times higher tumor uptake compared to the non-targeted niosomes coated with PEG polymer. Long circulation time and uniform bio-distribution throughout the entire tumor make pHLIP-coated niosomes to be an attractive novel delivery system.

## **Introduction**

Most of the currently approved nanomedicinal products for cancer imaging and therapy are non-targeted nanovectors that accumulate in the tumor tissues purely through the enhanced permeability and retention (EPR) effect (Dawidczyk et al., 2014). It is nearly impossible to find a universal targeting moiety for cancers as they are heterogeneous (Stingl and Caldas, 2007, Weigelt et al., 2005). At the same time, extracellular acidity has been identified as a general property of cancerous cells and especially the most aggressive ones (Stubbs et al., 2000, Calorini et al., 2012). Family of pH (Low) Insertion Peptides (pHLIP® peptides) are under development as novel agents, which target tumor acidity (Andreev et al., 2009, Weerakkody et al., 2013). The peptides sense pH at the surface of cancer cells, where it is the lowest (Anderson et al., 2016), and insert into cellular membranes (Reshetnyak et al., 2006, Reshetnyak et al., 2007, Reshetnyak et al., 2008, Andreev et al., 2010). Nanocarriers decorated with pHLIPs are biocompatible, can target tumor and demonstrate enhanced cellular uptake by cancer cells (Du et al., 2014, Wijesinghe et al., 2013, Yao et al., 2013b, Arachchige et al., 2015, Yao et al., 2013a). In addition to pHLIP-coated nanoparticles, nanocarriers containing pH-sensitive polymers and lipids were known for decades (Chu et al., 1990, Subbarao et al., 1987, Karanth and Murthy, 2007, Lee et al., 1998).

In this study we introduced pHLIP-coated niosomes. Niosomes are self-assembled bilayer vesicles analogous to liposomes, comprised of surfactants of Span®, Tween® or Brij® series (Rajera et al., 2011). Similar to liposomes, niosomes are used to encapsulate both hydrophilic and lipophilic drugs. At the same time, non-ionic surfactant vesicles, niosomes, are cheaper in production, have longer shelf lives

compared to liposomes, and bilayer fluidity and microviscosity could be easily modulated (Moghassemi and Hadjizadeh, 2014, Marianecci et al., 2014, Lohumi, 2012, Karim et al., 2010). Sorbitan esters (Spans®) are FDA approved for use in food processing and pharmaceuticals (Cottrell and van Peij, 2004). They are safe, amphiphilic compounds derived from sorbitol (i.e., a synthetic sweetener). Span20 mostly consists of a fully saturated short alkyl chain (lauryl - C12). The single carbon bonds in Span20 allow the alkyl chain to pack tightly, resulting in the smallest and stable niosomes, oppose to the niosomes consisting of longer chain surfactants, Spans40-80 (Lo et al., 2010, Hao et al., 2002, Israelachvili et al., 1980). Vesicles prepared by Span-series surfactants have been reported to be viable drug carriers for different diseases and different routes of administration (Ghanbarzadeh et al., 2015, Balakrishnan et al., 2009, Sahoo et al., 2014, Liu et al., 2017, Ammar et al., 2011, Guinedi et al., 2005, Hunter et al., 1988, Jadon et al., 2009, Pardakhty et al., 2007). In this study we introduced novel formulations, pHLP-coated niosomes, comprised of Span20 surfactant and cholesterol.

## **Materials and Methods**

### ***Materials***

Sorbitan monolaurate (Span20); cholesterol  $\geq 99\%$ ; N-(2-Hydroxyethyl)piperazine-N'-(2-ethanesulfonic acid) (HEPES)  $\geq 99.5\%$  and N-(1-Pyrenyl)maleimide (Pyr-maleimide) were purchased from Sigma-Aldrich. 1,2-dioleoyl-sn-glycero-3-phosphoethanolamine-N-[4-(p-maleimidophenyl)butyramide] sodium salt (DSPE-maleimide) and 1,2-distearoyl-sn-glycero-3-phosphoethanolamine-N-[carboxy(polyethylene glycol)-2000] ammonium salt (DSPE-PEG(2000)) were obtained from Avanti Polar Lipids. Octadecyl Rhodamine B chloride (R18) was

purchased from Thermo Fisher Scientific. The wild type (WT) pH (Low) Insertion Peptide: ACEQNPIYWARYADWLFTTPLLALLVDADEGT was prepared by solid-phase peptide synthesis and purified at the C.S. Bio. All other chemicals used in the study were of the highest purity and all solvents were of spectroscopic grade. Water was purified through a Millipore Milli-Q system.

### ***Synthesis of DSPE-pHLIP and Pyr-pHLIP***

pHLIP was conjugated with Pyr-maleimide or DSPE-maleimide in methanol. 5 mg of peptide dissolved in 250  $\mu$ L methanol (blown with argon) and Pyr-maleimide or DSPE-maleimide (from 9.9 mM stock solution) dissolved in chloroform was mixed at a molar ratio 1:1. Reaction mixture was kept at room temperature for about 2-6 hours until the conjugation was completed. The Pyr-pHLIP product formation was monitored by the reversed phase (Zorbax SB-C18 columns, 4.6  $\times$  250 mm 5  $\mu$ m, Agilent Technology) high-performance liquid chromatography (RP-HPLC) using a gradient from 25-75% acetonitrile in water containing 0.05% trifluoroacetic acid (TFA). The Pyr-pHLIP product was characterized by SELDI-TOF mass spectrometry (Pyr-pHLIP expected MW 4409.0, found 4401.7, Figure S1). The concentration of Pyr-pHLIP conjugate was determined by absorbance using the molar extinction coefficient for Pyr:  $339=40,000 \text{ M}^{-1} \cdot \text{cm}^{-1}$ . The reaction progress in conjugation of DSPE with pHLIP was monitored by the RP-HPLC using a gradient from 25-80% acetonitrile in water containing 0.05% TFA by monitoring a decrease of peak corresponding to the unlabeled pHLIP in the reaction mixture. The concentration of DSPE-pHLIP conjugate was determined by absorbance using the molar extinction coefficient for pHLIP:  $280=13,940 \text{ M}^{-1} \cdot \text{cm}^{-1}$ .

### *Niosomes preparation*

10 mM stock solutions of Span20 and cholesterol were prepared by dissolving the products in chloroform and methanol mixture of 3:1 (v/v). pHLIP-coated niosomes were prepared by mixing solutions of the 43 mol% of Span20, 50 mol% of cholesterol, 5 mol% of DSPE-pHLIP or Pyr-pHLIP and 2 mol% of R18. PEG-coated niosomes were prepared by mixing solutions of the 43 mol% of Span20, 50 mol% of cholesterol, 5 mol% of DSPE-PEG and 2 mol% of R18. Some preparations of niosomes used for fluorescence spectroscopy measurements, hemolysis and plasma stability studies contained no R18 and comprised of 45 mol% of Span20, 50 mol% of cholesterol, 5 mol% of Pyr-pHLIP, or DSPE-pHLIP, or DSPE-PEG. Solutions containing all components were evaporated in the flask covered with aluminum foil for 1 hour on rotary evaporator at 60°C producing an even thin film, followed by additional 1 hour evaporation under the high vacuum to remove traces of organic solvents. The layers were hydrated in 2 mL of preheated for 60°C 10 mM PBS or HEPES buffer solutions, pH 7.4 containing 137 mM NaCl, 2.7 mM KCl and 1 mM CaCl<sub>2</sub>. To disrupt large particles and obtain monodisperse solution of nanoparticles we employed both sonication and extrusion. The sonication and extrusion protocols were optimized varying power and duration of sonication, as well as adjusting extrusion approach. According to the optimized protocol niosome solution was sonicated using the probe sonicator VirTis (VirSonic 100) for approximately 5 minutes at 60°C at output power of 8-10 Watts, followed by consequential extrusion (31 times) using 200 nm, 100 nm and 50 nm filters. Niosome solution was sterilized by filtering through 0.2 µm filter. The concentration was calculated by measuring absorbance of R18 at 546 nm ( $\epsilon_{546}=104,126 \text{ M}^{-1} \text{ cm}^{-1}$ ) or pHLIP at 280 nm ( $\epsilon_{280}=13,940 \text{ M}^{-1} \text{ cm}^{-1}$ ) of the niosomes dissolved in methanol.

Niosomes were stored at 4°C.

### ***Size and Zeta potential measurements***

The size distribution of niosomes was measured by dynamic light scattering (DLS) using a Zetasizer Nano ZS (Malvern) instrument and a nanoparticle tracking system, Nanosight (NS300, Malvern). The zeta (  $\zeta$  ) potential was measured on a Zetasizer Nano ZS instrument using folded capillary cells from Malvern.

### ***Fluorescence measurements***

Steady-state fluorescence measurements were carried out under a temperature control at 25 °C on a PC1 spectrofluorometer (ISS, Inc.). The concentration of the pyrene was 12.5  $\mu$ M. Pyrene fluorescence was excited at 333 nm and recorded in the range of 350-500 nm. The polarizers in the excitation and emission paths were set at the “magic” angle (54.7° from the vertical orientation) and vertically (0°), respectively.

### ***Cryo-electron microscopy***

Niosome solution (5  $\mu$ L droplet) was spread on a Lacey formar/carbon electron microscopy grid and preserved in a frozen-hydrated state by a rapid freezing in liquid ethane. The vitrification process was performed using FEI Vitrobot system with the setting of a single blot of 3 sec, an offset of 1, and drain and waiting time of 1 sec. Transmission electron microscopy (TEM) (JEOL 2100) with an accelerating voltage of 200 kV at magnifications in the range of 10,000x to 150,000x was used to image niosomes to establish the shape, size, and homogeneity of the particles. Size histograms were fitted with a Gauss function.

### ***Cell lines***

Lung carcinoma A549 and mouse mammary 4T1 cell lines were obtained from American Type Culture Collection (ATCC). Cells were authenticated, stored according to the supplier's instructions, and used within 3-4 months after frozen aliquots resuscitations. Cells were cultured in Dulbecco's Modified Eagle's Medium (DMEM) and Roswell Park Memorial Institute Medium (RPMI) supplemented with 10% fetal bovine serum (FBS), 0.1% of 10 µg/mL of ciprofloxacin (Cipro) in a humidified atmosphere of 5% CO<sub>2</sub> and 95% air at 37°C.

### ***Cell proliferation assay***

A549 and 4T1 cells were seeded in 96 well-plates (~3,000 cells per well) at pH 7.4. The following day, cells were treated for 2 hours with increasing concentrations of pHLIP-coated niosomes (0, 10, 50, 100, 250, 500 and 1000 µM of Span20) in serum free DMEM media at pH 7.4, followed by addition of an equal volume of medium with 20% (v/v) FBS. In another experiment, after 2 hours of cells treatment with pHLIP-coated niosomes, the solution was replaced by media containing 10% FBS. Cells were grown for 3 days until non-treated cells in control reached 80-90% confluence. Cell viability was assessed by the colorimetric reagent (CellTiter 96 AQueousOne Solution Assay, Promega) of the MTS (3-(4,5-dimethylthiazol-2-yl)-5-(3-carboxymethoxyphenyl)-2-(4-sulfophenyl)-2H-tetrazolium) assay, which was added for 1 hour to cells followed by measuring absorbance at 490 nm. All samples were prepared in triplicate. Each experiment was repeated several times.

### ***Hemolysis assay***

Single donor human whole blood was purchased from Innovative Research. Red blood cells (RBCs) were collected by centrifugation of whole blood at 2000 rpm for 10 minutes followed by washing three times with Dulbecco's PBS (DPBS) and re-suspended in DPBS at a concentration of 7.5% (v:v). Varying concentrations of niosomes (from 50  $\mu$ M up to 400  $\mu$ M) in 10 mM HEPES buffer, pH 7.4 containing 137 mM NaCl, 2.7 mM KCl, 1 mM CaCl<sub>2</sub> were added to RBCs to form 5% RBC suspension. The resultant mixtures were incubated at 37°C for 2 hours and then centrifuged at 2000 rpm for 10 min. The hemolysis was assessed by the release of hemoglobin, which was monitored by measuring of absorbance at 450 nm. 10 mM HEPES buffer, pH 7.4 containing 137 mM NaCl, 2.7 mM KCl, 1 mM CaCl<sub>2</sub> and DPBS were used as negative controls. As positive controls, which result in 100% lysis of RBCs, we used i) water and ii) 10% of Triton X-100. The percentage of hemolysis was calculated as follows:

$$\% \text{ Hemolysis} = 100 \cdot \frac{OD_{Test} - OD_{NC}}{OD_{PC} - OD_{NC}}$$

where, OD<sub>Test</sub>, OD<sub>NC</sub>, and OD<sub>PC</sub> are the optical density reading (absorbance) values of the test sample, negative control and positive control, respectively. The assay was performed in triplicate on niosomes with and without R18.

### ***Stability in plasma***

Plasma was separated from the single donor human whole blood by centrifugation of

whole blood at 2000 rpm for 10 minutes and collecting of supernatant. Varying concentrations of niosomes (from 50  $\mu$ M up to 400  $\mu$ M) in 10 mM HEPES buffer, pH 7.4 containing 137 mM NaCl, 2.7 mM KCl, 1 mM CaCl<sub>2</sub> were added to plasma and incubated at 37°C. The stability of niosomes was assessed by monitoring size of niosomes measured using a nanoparticle tracking system, Nanosight (NS300, Malvern) before mixing with plasma and at 0, 2 and 24 hours after the treatment with plasma.

### ***Cellular uptake of niosomes***

A549 and 4T1 cells (~500,000 cells) in suspension were treated with 500  $\mu$ M R18 labelled pHLIP-coated niosomes at pH 7.8 and pH 5.5 for about 1 hour at 37°C in serum free DMEM media. We used DMEM containing no sodium bicarbonate and adjusted pH by HCl or NaOH. After incubation period, cells were pelleted by centrifugation (2500 rpm, 2.5 min) at room temperature. The supernatant was removed and the cell pellet was re-suspended in 1 mL of fresh PBS pH 7.4 and centrifuged for the second time. The second cell pellet was re-suspended in PBS pH 7.4 with or without addition of Trypan Blue solution (Sigma-Aldrich). The 20  $\mu$ L of the cell suspension solution was loaded into a counting chamber. The cellular uptake of fluorescent niosomes was assessed by counting of fluorescent cells using Nexcelom cellometer at 525 nm excitation and 595 nm emission channels.

### ***Fluorescence microscopy***

In separate experiment, A549 and 4T1 cells (~500,000 cells) in suspension were treated with 500  $\mu$ M R18 labelled pHLIP-coated niosomes at pH 6.4 (or normal pH 7.4) for 1 hour at 37°C serum free media and followed by the described above steps of cell

washing. After washing, the cell pellet was re-suspended and cells were seeded in glass bottom collagen coated cell dishes (MatTek). The phase contrast and fluorescence images from cells were recorded at 0, 4 and 24 hours under an inverted epi-fluorescence microscope (Olympus IX71) using a 20x and 40x objective lenses.

### ***Tumor mouse model***

All animal studies were conducted according to the animal protocol AN07-01-015 approved by the Institutional Animal Care and Use Committee at the University of Rhode Island, in compliance with the principles and procedures outlined by NIH for the Care and Use of Animals. 4T1 mammary tumors were established by subcutaneous injection of 4T1 cells ( $1 \times 10^6$  cells/mL, 0.1 mL/flank) in the right flank of adult female BALB/c mice (about 20-25 g weight) obtained from Envigo RMS, Inc. For this study, 34 mice were used including controls.

### ***Ex vivo fluorescence imaging***

When tumors reached 6-8 mm in diameter different constructs of niosomes containing 2 mol% of fluorescent R18 were given as a single tail vein injection (100  $\mu$ L of 50  $\mu$ M of R18). Animals were euthanized at 4, 24 and 48 hours post-injection. Necropsy was performed immediately after euthanization. The Supplementary Tables S1 and S2 contain information about the number of animals used for each fluorescently-labeled niosomes for each time point. Tumors, kidneys, liver and muscles were collected for imaging on a FX Kodak in-vivo image station connected to the Andor CCD. The imaging was performed using excitation and emission filters with a band of transmittance at  $540 \pm 20$  nm and  $605 \pm 20$  nm, respectively. The mean fluorescence

intensities of tumor and organs were calculated using ImageJ software.

### ***Imaging of tumor sections***

Frozen tumor tissues were sectioned at a thickness of 5  $\mu\text{m}$  using a Vibratome UltraPro 5000 Cryostat. Sections were mounted on microscope slides, dried in air, and washed with deionized water. Tumor sections mounted on microscopic slides were directly incubated with 1 mM DAPI solution in PBS at 37°C for about 10 minutes and washed with PBS solution to remove excess of the dye. Frozen tumor sections with R18 contained pHLIP-coated niosomes were analyzed without further processing using Zeiss LSM 700 confocal module under DAPI and Rhodamine channels using a 20x objective lens. Following fluorescence imaging, the adjacent sections were then stained with hematoxylin and eosin (H&E) and imaged under microscope.

### **Results**

We introduced two formulations of pHLIP coated niosomes. In both cases the major components of niosome content was Span20 (varied in the range of 43-45 mol%) and cholesterol (50 mol%), and in some niosome formulations we also used fluorescent R18 (0-2 mol%). pHLIP was conjugated either with DSPE lipids (DSPE-pHLIP) or hydrophobic fluorescent dye, pyrene, (Pyr-pHLIP) and introduced into niosomes at amount of 5 mol%. These formulations represent two different approaches for introducing pHLIP into niosome coating: i) pHLIP conjugated with the lipid headgroup as it was done previously (Wijesinghe et al., 2013) and ii) pHLIP conjugated to various hydrophobic molecules, such as pyrene, which have high affinity to membrane and can intercalate into bilayer. There is an advantage of using pyrene over DSPE lipids, since

i) progression of conjugation reaction of pHLIP with pyrene is easy to monitor by HPLC and mass-spectrometry; ii) incorporation of Pyr-pHLIP into niosomes could be assessed by measuring changes of pyrene fluorescence (see below); and iii) pyrene could be used for intercalation into bilayers of various thicknesses.

The cryo-TEM imaging confirmed unilamellar structure of pHLIP-coated niosomes (Figure 1a, b). The multiple cryo-TEM images were analyzed to plot size-distribution histograms, which were fitted by Gauss functions (Figure S2). The mean and standard deviations of Gaussian distributions for DSPE-pHLIP and Pyr-pHLIP coated niosomes were established to be  $65.2 \pm 15.3$  nm and  $52.2 \pm 10.1$  nm, respectively (Table 1). The hydrodynamic diameter of DSPE-pHLIP and Pyr-pHLIP coated niosomes in solution were  $89.7 \pm 7.1$  nm and  $72.6 \pm 3.3$  nm, respectively. The zeta potential of DSPE-pHLIP and Pyr-pHLIP coated niosomes was  $-35.4$  mV and  $-31.3$  mV, respectively. When Pyr-pHLIP was incorporated into niosomes the fluorescence spectra of pyrene was altered compared to the pyrene emission in methanol (the niosome formulation used for fluorescence measurements did not contain fluorescent R18) (Figure 1c). It was observed appearance of the characteristic excimer fluorescence at 440-500 nm, which is indicative of the stacking of pyrene rings within the bilayer of niosomes.

We investigated shelf lifetime of pHLIP coated niosomes. The formulations were kept in buffer solution of pH 7.4 refrigerated at  $4^{\circ}\text{C}$  for a month. The size of particles remained unchanged in solution during 30 days, while the values of zeta potential decreased on about 40% (from negative 30–35 mV to negative 47–53 mV) (Figure S3). The changes of zeta potential, which were not associated with changes of particle

size, might be attributed to the oxidation of the components of Span20 mixture forming negatively charged species and enhancing an overall negative charge of niosomes (de Sousa Lobato et al., 2013, Kishore et al., 2011, Smith, 1981, Kerwin, 2008).

The cytotoxicity of the pHLIP-coated niosomes was tested on murine 4T1 mammary cancer cells and human lung A549 carcinoma cells. The data indicate that DSPE-pHLIP and Pyr-pHLIP niosomes do not show toxicity for cells. The pH-dependent cellular uptake of the fluorescent pHLIP-coated niosomes containing 2 mol% of R18 was assessed by quantifying rhodamine fluorescence taken by cells. Cells were treated with R18 containing niosomes at pH 7.8 and pH 5.5 for 1 hour. We choose to treat cells with constructs at pH7.8, which is slightly above than normal physiological pH7.4, since it was shown that pH at the surface of cancer cells, especially highly metastatic cancer cells such as 4T1, is lower even when pH of media is normal (Anderson et al., 2016). We also choose to treat cells with constructs at pH5.5, which is slightly lower than mean pH established at the surface of cancer cells within tumors, pH6.0, (Anderson et al., 2016) with main goal to enhance difference in cellular uptake of niosomes in this model experiment. The fluorescent signal from the cells treated with niosomes was analyzed using cellometer (Figure 2). We also used cell impermeable dye, Trypan Blue, to quench fluorescent signal outside of cells or at the outer leaflet of lipid bilayer of plasma membrane to prove that fluorescent signal is associated with cellular uptake of niosomes. It is known that Trypan Blue is used to quench fluorescence in the range of 580 620 nm (Nuutila and Lilius, 2005). The uptake of the fluorescent niosomes coated with both DSPE-pHLIP and Pyr-pHLIP by 4T1 and A549 cancer cells was from 2 to 9 times higher at low pH compared to the uptake at treatment pH of 7.8 (established with high

statistical significance, p-levels determined by the two-tailed unpaired Student's t-test were less than 0.0001). Addition of Trypan Blue to cells led to the quenching of rhodamine fluorescence. More detailed information about cellular fluorescence after the treatment with niosomes is presented in Figure S4.

Next, we investigated distribution of the fluorescent niosomes within A549 and 4T1 cancer cells. Cells were treated with R18 fluorescent niosomes at low pH (pH6.4) for 1 hour, followed by washing, seeding cells in glass bottom collagen coated cell dishes and imaging. The fluorescent signal of DSPE-pHLIP and Pyr-pHLIP coated niosomes in A549 cells (Figure 3) and 4T1 cells (Figure S5) were distributed through cells, most probably in endosomes and lysosomes. The data confirmed pH-dependent cellular uptake of pHLIP-coated niosomes.

Finally, our goal was to investigate tumor targeting and distribution of pHLIP-coated niosomes, which we compared with the control niosomes coated with PEG polymer that accumulate in tumors due to the EPR effect. Before proceeding to animal studies we investigate stability of pHLIP and PEG coated niosome formulations in plasma, and calculated percentage of hemolysis. RBCs and plasma were separated from human blood samples. RBCs were treated with two sets of increasing concentrations of pHLIP and PEG coated niosomes with and without R18 for 2 hours at 37°C. The lysis of RBCs was less than 1% in the case of use of DSPE-pHLIP and Pyr-pHLIP coated niosomes and less than 2% for DSPE-PEG coated niosomes. Also, stability of pHLIP and PEG coated niosomes with and without R18 were investigated for 24 hours in plasma separated from the blood. The size of all niosome formulations (DSPE-pHLIP, Pyr-

pHLIP and DSPE-PEG) was not altered indicating on their stability in blood.

The tumor targeting of the fluorescent R18 containing DSPE-pHLIP and Pyr-pHLIP coated niosomes were investigated in mice. Fluorescent niosomes were given as a single tail vein injection, animals were euthanized at different time points post-injection (4, 24 and 48 hours). Main organs were collected, cut in half and imaged (Figure 4 and Table S1). At 24 hours we observed peak in tumor uptake of the fluorescent niosomes. The mean tumor to muscle ratio within 48 hours was found to be  $4.9 \pm 1.3$  and  $6.8 \pm 1.4$  for DSPE-pHLIP and Pyr-pHLIP coated niosomes, respectively. The signal in kidney was minimal, with some accumulation of the constructs in liver. Uptake of pHLIP-coated niosomes by tumor, muscle, kidney and liver at 24 hours post-injection was compared with the uptake of PEG-coated niosomes. Figure 5a shows representative images of tumor and organs obtained from mice injected with different constructs and Figure 5b (and Table S2) reflects quantitative uptake of the constructs by the tumors and organs. Tumor-targeting niosomes coated with pHLIP exhibited 2.1-2.7 times higher tumor uptake compared to the non-targeted niosomes coated with PEG polymer. Figure 6 demonstrates cellular distribution of fluorescent signal within the tumor mass. The sections were obtained from the center of the tumors. The fluorescence is associated with cellular structures and no nuclear staining was observed as in the case of experiments on cultured cells.

## **Discussion**

The targeted delivery of nanomaterials is one of the most important aspects of successful development of nanotechnology and translation of nanomaterials to the clinics. Various

approaches are tested with moderate success. Our approach is based on targeting of tumor acidity by utilizing ability of pHLIPs to sense pH at the surface of cells. Acidosis is a general property of tumor microenvironment associated with tumor development and progressions (Fang et al., 2008, Gillies et al., 2008, Vander Heiden et al., 2009). Moreover, acidity is linked to other pathological states, such as ischemia, atherosclerosis, stroke (Rajamäki et al., 2013, Koo et al., 1993, Mizock and Falk, 1992). It was shown that nanoparticles coated with pHLIP promote targeting and cellular uptake of these nanoparticles (Wijesinghe et al., 2013, Yao et al., 2013b, Yao et al., 2013a, Wei et al., 2017, Janic et al., 2016, Tian et al., 2017, Emmetiere et al., Han et al., 2013, Yu et al., 2016, Yu et al., 2015). Previously, we demonstrated that pHLIP-coated liposomes capable to fuse with cellular membranes and promote delivery hydrophobic cargo molecules to cellular membranes, and hydrophilic payloads to cytoplasm of cancer cells (Yao et al., 2013b). In this work we tested surfactant- and cholesterol-based niosomes. The pHLIP-coated niosomes were smaller in size and more stable compared to the pHLIP-coated liposomes. pHLIP-coated niosomes demonstrated pH-dependent cellular uptake and excellent tumor targeting. Control non-targeted PEG-coated niosomes exhibited 2-3 times less tumor accumulation. Targeting of acidic tumors occurs due to the ability of pHLIPs to insert into cellular membranes in environment of low extracellular pH. Thus, at low pH, pHLIPs behave as fusogenic peptides, which bring the niosome membrane in close contact to the cellular membrane. There are two main possibilities of pHLIP-coated niosome's cellular entry. Either pHLIP-coated niosomes might fuse directly with the plasma membrane of cancer cells in environment of low pH and/or niosomes can be taken up into the cell via endocytotic pathways, more favorably, via micropinocytosis due simultaneous insertions of multiple pHLIPs into the cellular

membrane. Niosomes, which are internalized into cell via endocytosis might fuse with the endosomal membrane at low pH. In either case, niosomes carrying lipophilic and/or hydrophilic drugs can effectively enter into the cells in a pH-dependent manner.

The pHLIP-coated liposomes and niosomes follow a closely similar mechanism utilized by viruses and pathogenic organisms to enter into a cell. In contrast to liposomes, niosomes are smaller in size, they demonstrate prolong shelf life, very good tumor targeting and distribution within tumor, and their manufacturing cost is lower. On other hand, niosome's encapsulation capacity is lower and different combinations of surfactants are needed for entrapment of various hydrophobic molecules within their bilayer to preserve overall stability of nano-vesicles. Different formulations might find utility for different therapeutic purposes.

## **Acknowledgements**

We would like to thank Dr. Al Bach and Kim Andrews, Rhode Island IDEa Network for Excellence in Biomedical Research (INBRE), for their assistance in using the cello meter; Dr. Richard Kingsley and Dr. Iftheker Khan, University of Rhode Island, for performing TEM imaging; Mr Paul W Johnson, RI Genomic and Sequencing Center for his assistance in confocal microscopy, Dr. Dammika Weerakkody, University of Rhode Island for his assistance on biophysical instrumentation and Mr. Troy Crawford, University of Rhode Island for his assistance in animal studies. This work was supported by the General Medical Sciences of the National Institutes of Health grant R01GM073857 to OAA and YKR. Also, this research was supported in part by an Institutional Development Award (IDeA) Network for Biomedical Research Excellence from the National Institute of General Medical Sciences of the National Institutes of Health under grant number P20GM103430.

## **Declaration of Interest**

OA Andreev and YK Reshetnyak have founded and have a financial interest in a company, pHLIP, Inc., with the aim of bringing pHLIP technology to the clinic. The company has had no involvement in funding the studies reported here.

## References

1. AMMAR, H., GHORAB, M., EL-NAHHAS, S. & HIGAZY, I. 2011. Proniosomes as a carrier system for transdermal delivery of tenoxicam. *International journal of pharmaceutics*, 405, 142-152.
2. ANDERSON, M., MOSHNIKOVA, A., ENGELMAN, D. M., RESHETNYAK, Y. K. & ANDREEV, O. A. 2016. Probe for the measurement of cell surface pH in vivo and ex vivo. *Proc Natl Acad Sci U S A*, 113, 8177-81.
3. ANDREEV, O. A., ENGELMAN, D. M. & RESHETNYAK, Y. K. 2009. Targeting acidic diseased tissue: New technology based on use of the pH (Low) Insertion Peptide (pHLIP). *Chimica oggi*, 27, 34.
4. ANDREEV, O. A., ENGELMAN, D. M. & RESHETNYAK, Y. K. 2010. pH-sensitive membrane peptides (pHLIPs) as a novel class of delivery agents. *Molecular membrane biology*, 27, 341-352.
5. ARACHCHIGE, M. C., RESHETNYAK, Y. K. & ANDREEV, O. A. 2015. Advanced targeted nanomedicine. *Journal of biotechnology*, 202, 88-97.
6. BALAKRISHNAN, P., SHANMUGAM, S., LEE, W. S., LEE, W. M., KIM, J. O., OH, D. H., KIM, D.-D., KIM, J. S., YOO, B. K. & CHOI, H.-G. 2009. Formulation and in vitro assessment of minoxidil niosomes for enhanced skin delivery. *International journal of pharmaceutics*, 377, 1-8.
7. CALORINI, L., PEPPICELLI, S. & BIANCHINI, F. 2012. Extracellular acidity as favouring factor of tumor progression and metastatic dissemination. *Exp Oncol*, 34, 79-84.

8. CHU, C.-J., DIJKSTRA, J., LAI, M.-Z., HONG, K. & SZOKA, F. C. 1990. Efficiency of cytoplasmic delivery by pH-sensitive liposomes to cells in culture. *Pharmaceutical research*, 7, 824-834.
9. COTTRELL, T. & VAN PEIJ, J. 2004. 7 Sorbitan esters and polysorbates. *Emulsifiers in food technology*, 162.
10. DAWIDCZYK, C. M., RUSSELL, L. M. & SEARSON, P. C. 2014. Nanomedicines for cancer therapy: state-of-the-art and limitations to pre-clinical studies that hinder future developments. *Front Chem*, 2, 69.
11. DE SOUSA LOBATO, K. B., PAESE, K., FORGEARINI, J. C., GUTERRES, S. S., JABLONSKI, A. & DE OLIVEIRA RIOS, A. 2013. Characterisation and stability evaluation of bixin nanocapsules. *Food chemistry*, 141, 3906-3912.
12. DU, J.-Z., MAO, C.-Q., YUAN, Y.-Y., YANG, X.-Z. & WANG, J. 2014. Tumor extracellular acidity-activated nanoparticles as drug delivery systems for enhanced cancer therapy. *Biotechnology advances*, 32, 789-803.
13. EMMETIERE, F., IRWIN, C., VIOLA-VILLEGAS, N., LONGO, V., CHEAL, S., ZANZONICO, P., PILLARSETTY, N., WEBER, W., LEWIS, J. & REINER, T. F-Labeled-Bioorthogonal Liposomes for. *Vivo*.
14. FANG, J. S., GILLIES, R. D. & GATENBY, R. A. Adaptation to hypoxia and acidosis in carcinogenesis and tumor progression. *Seminars in cancer biology*, 2008. Elsevier, 330-337.
15. GHANBARZADEH, S., KHORRAMI, A. & ARAMI, S. 2015. Nonionic surfactant-based vesicular system for transdermal drug delivery. *Drug delivery*, 22, 1071-1077.

16. GILLIES, R. J., ROBEY, I. & GATENBY, R. A. 2008. Causes and consequences of increased glucose metabolism of cancers. *Journal of Nuclear Medicine*, 49, 24S-42S.
17. GUINEDI, A. S., MORTADA, N. D., MANSOUR, S. & HATHOUT, R. M. 2005. Preparation and evaluation of reverse-phase evaporation and multilamellar niosomes as ophthalmic carriers of acetazolamide. *International Journal of Pharmaceutics*, 306, 71-82.
18. HAN, L., MA, H., GUO, Y., KUANG, Y., HE, X. & JIANG, C. 2013. pH-Controlled Delivery of Nanoparticles into Tumor Cells. *Advanced healthcare materials*, 2, 1435-1439.
19. HAO, Y., ZHAO, F., LI, N., YANG, Y. & LI, K. A. 2002. Studies on a high encapsulation of colchicine by a niosome system. *International journal of pharmaceutics*, 244, 73-80.
20. HUNTER, C., DOLAN, T., COOMBS, G. & BAILLIE, A. 1988. Vesicular systems (niosomes and liposomes) for delivery of sodium stibogluconate in experimental murine visceral leishmaniasis. *Journal of pharmacy and pharmacology*, 40, 161-165.
21. ISRAELACHVILI, J., MARČELJA, S. & HORN, R. 1980. Physical principles of membrane organization. *Quarterly reviews of biophysics*, 13, 121-200.
22. JADON, P. S., GAJBHIYE, V., JADON, R. S., GAJBHIYE, K. R. & GANESH, N. 2009. Enhanced oral bioavailability of griseofulvin via niosomes. *AAPS PharmSciTech*, 10, 1186.
23. JANIC, B., BHUIYAN, M. P., EWING, J. R. & ALI, M. M. 2016. pH-

- Dependent cellular internalization of paramagnetic nanoparticle. *ACS sensors*, 1, 975.
24. KARANTH, H. & MURTHY, R. 2007. pH-sensitive liposomes-principle and application in cancer therapy. *Journal of pharmacy and pharmacology*, 59, 469-483.
  25. KARIM, K. M., MANDAL, A. S., BISWAS, N., GUHA, A., CHATTERJEE, S., BEHERA, M. & KUOTSU, K. 2010. Niosome: a future of targeted drug delivery systems. *Journal of advanced pharmaceutical technology & research*, 1, 374.
  26. KERWIN, B. A. 2008. Polysorbates 20 and 80 used in the formulation of protein biotherapeutics: structure and degradation pathways. *Journal of pharmaceutical sciences*, 97, 2924-2935.
  27. KISHORE, R. S., PAPPENBERGER, A., DAUPHIN, I. B., ROSS, A., BUERGI, B., STAEMPFLI, A. & MAHLER, H. C. 2011. Degradation of polysorbates 20 and 80: Studies on thermal autoxidation and hydrolysis. *Journal of pharmaceutical sciences*, 100, 721-731.
  28. KOO, B., BECKER, L. E., CHUANG, S., MERANTE, F., ROBINSON, B. H., MACGREGOR, D., TEIN, I., HO, V. B., MCGREAL, D. A. & WHERRETT, J. R. 1993. Mitochondrial encephalomyopathy, lactic acidosis, stroke-like episodes (MELAS): Clinical, radiological, pathological, and genetic observations. *Annals of neurology*, 34, 25-32.
  29. LEE, R. J., WANG, S., TURK, M. J. & LOW, P. S. 1998. The effects of pH and intraliposomal buffer strength on the rate of liposome content release and intracellular drug delivery. *Bioscience reports*, 18, 69-78.

30. LIU, H., TU, L., ZHOU, Y., DANG, Z., WANG, L., DU, J., FENG, J. & HU, K. 2017. Improved Bioavailability and Antitumor Effect of Docetaxel by TPGS Modified Proniosomes: In Vitro and In Vivo Evaluations. *Scientific Reports*, 7.
31. LO, C. T., JAHN, A., LOCASCIO, L. E. & VREELAND, W. N. 2010. Controlled self-assembly of monodisperse niosomes by microfluidic hydrodynamic focusing. *Langmuir*, 26, 8559-8566.
32. LOHUMI, A. 2012. A novel drug delivery system: niosomes review. *Journal of drug delivery and therapeutics*, 2.
33. MARIANECCI, C., DI MARZIO, L., RINALDI, F., CELIA, C., PAOLINO, D., ALHAIQUE, F., ESPOSITO, S. & CARAFA, M. 2014. Niosomes from 80s to present: the state of the art. *Advances in colloid and interface science*, 205, 187-206.
34. MIZOCK, B. A. & FALK, J. L. 1992. Lactic acidosis in critical illness. *Critical care medicine*, 20, 80-93.
35. MOGHASSEMI, S. & HADJIZADEH, A. 2014. Nano-niosomes as nanoscale drug delivery systems: an illustrated review. *Journal of Controlled Release*, 185, 22-36.
36. NUUTILA, J. & LILIUS, E. M. 2005. Flow cytometric quantitative determination of ingestion by phagocytes needs the distinguishing of overlapping populations of binding and ingesting cells. *Cytometry A*, 65, 93-102.
37. PARDAKHTY, A., VARSHOSAZ, J. & ROUHOLAMINI, A. 2007. In vitro study of polyoxyethylene alkyl ether niosomes for delivery of insulin.

International journal of pharmaceutics, 328, 130-141.

38. RAJAMÄKI, K., NORDSTRÖM, T., NURMI, K., ÅKERMAN, K. E., KOVANEN, P. T., ÖÖRNI, K. & EKLUND, K. K. 2013. Extracellular acidosis is a novel danger signal alerting innate immunity via the NLRP3 inflammasome. *Journal of Biological Chemistry*, 288, 13410-13419.
39. RAJERA, R., NAGPAL, K., SINGH, S. K. & MISHRA, D. N. 2011. Niosomes: a controlled and novel drug delivery system. *Biological and Pharmaceutical Bulletin*, 34, 945-953.
40. RESHETNYAK, Y. K., ANDREEV, O. A., LEHNERT, U. & ENGELMAN, D. M. 2006. Translocation of molecules into cells by pH-dependent insertion of a transmembrane helix. *Proceedings of the National Academy of Sciences*, 103, 6460-6465.
41. RESHETNYAK, Y. K., ANDREEV, O. A., SEGALA, M., MARKIN, V. S. & ENGELMAN, D. M. 2008. Energetics of peptide (pHLIP) binding to and folding across a lipid bilayer membrane. *Proceedings of the National Academy of Sciences*, 105, 15340-15345.
42. RESHETNYAK, Y. K., SEGALA, M., ANDREEV, O. A. & ENGELMAN, D. M. 2007. A monomeric membrane peptide that lives in three worlds: in solution, attached to, and inserted across lipid bilayers. *Biophysical journal*, 93, 2363-2372.
43. SAHOO, R. K., BISWAS, N., GUHA, A., SAHOO, N. & KUOTSU, K. 2014. Nonionic surfactant vesicles in ocular delivery: innovative approaches and perspectives. *BioMed research international*, 2014.
44. SMITH, L. L. 1981. *Cholesterol autoxidation*, Springer Science & Business

Media.

45. STINGL, J. & CALDAS, C. 2007. Molecular heterogeneity of breast carcinomas and the cancer stem cell hypothesis. *Nature Reviews Cancer*, 7, 791-799.
46. STUBBS, M., MCSHEEHY, P. M., GRIFFITHS, J. R. & BASHFORD, C. L. 2000. Causes and consequences of tumour acidity and implications for treatment. *Molecular medicine today*, 6, 15-19.
47. SUBBARAO, N. K., PARENTE, R. A., SZOKA JR, F. C., NADASDI, L. & PONGRACZ, K. 1987. The pH-dependent bilayer destabilization by an amphipathic peptide. *Biochemistry*, 26, 2964-2972.
48. TIAN, Y., ZHANG, Y., TENG, Z., TIAN, W., LUO, S., KONG, X., SU, X., TANG, Y., WANG, S. & LU, G. 2017. pH-Dependent Transmembrane Activity of Peptide-functionalized Gold Nanostars for Computed Tomography/Photoacoustic Imaging and Photothermal Therapy. *ACS Applied Materials & Interfaces*.
49. VANDER HEIDEN, M. G., CANTLEY, L. C. & THOMPSON, C. B. 2009. Understanding the Warburg effect: the metabolic requirements of cell proliferation. *science*, 324, 1029-1033.
50. WEERAKKODY, D., MOSHNIKOVA, A., THAKUR, M. S., MOSHNIKOVA, V., DANIELS, J., ENGELMAN, D. M., ANDREEV, O. A. & RESHETNYAK, Y. K. 2013. Family of pH (low) insertion peptides for tumor targeting. *Proceedings of the National Academy of Sciences*, 110, 5834-5839.
51. WEI, Y., LIAO, R., MAHMOOD, A. A., XU, H. & ZHOU, Q. 2017. pH-

Responsive pHLIP (pH Low Insertion Peptide) Nanoclusters of Superparamagnetic Iron Oxide Nanoparticles as a Tumor-selective MRI Contrast Agent. *Acta Biomaterialia*.

52. WEIGELT, B., PETERSE, J. L. & VAN'T VEER, L. J. 2005. Breast cancer metastasis: markers and models. *Nature reviews cancer*, 5, 591-602.
53. WIJESINGHE, D., ARACHCHIGE, M. C., LU, A., RESHETNYAK, Y. K. & ANDREEV, O. A. 2013. pH dependent transfer of nano-pores into membrane of cancer cells to induce apoptosis. *Scientific reports*, 3.
54. YAO, L., DANIELS, J., MOSHNIKOVA, A., KUZNETSOV, S., AHMED, A., ENGELMAN, D. M., RESHETNYAK, Y. K. & ANDREEV, O. A. 2013a. pHLIP peptide targets nanogold particles to tumors. *Proceedings of the National Academy of Sciences*, 110, 465-470.
55. YAO, L., DANIELS, J., WIJESINGHE, D., ANDREEV, O. A. & RESHETNYAK, Y. K. 2013b. pHLIP®-mediated delivery of PEGylated liposomes to cancer cells. *Journal of Controlled Release*, 167, 228-237.
56. YU, M., GUO, F., WANG, J., TAN, F. & LI, N. 2015. Photosensitizer-loaded pH-responsive hollow gold nanospheres for single light-induced photothermal/photodynamic therapy. *ACS applied materials & interfaces*, 7, 17592-17597.
57. YU, M., GUO, F., WANG, J., TAN, F. & LI, N. 2016. A pH-Driven and photoresponsive nanocarrier: Remotely-controlled by near-infrared light for stepwise antitumor treatment. *Biomaterials*, 79, 25-35.

## TABLES

**Table 1.** The center of Gauss distribution ( $D_{TEM}$ ) and the standard deviation obtained after fitting of histograms of niosome's diameter distributions (shown on Figure S2) calculated by analyzing cryo-TEM images. The mean hydrodynamic diameter ( $D_h$ ), the zeta potential ( $\zeta$ ) and the polydispersity index (PDI) were obtained from the dynamic light scattering measurements performed on niosomes in HEPES buffer at pH 7.4. DSPE-pHLIP and Pyr-pHLIP (5 mol%) coated Span20 (45 mol%) and cholesterol (50 mol%) niosomes were used.

<b>Construct</b>	<b><math>D_{TEM}</math>, nm</b>	<b><math>D_h</math>, nm</b>	<b><math>\zeta</math>, mV</b>	<b>PDI</b>
<b>DSPE-pHLIP</b>	65.2 ± 15.3	89.7 ± 7.1	-35.4 ± 2.3	0.19 ± 0.01
<b>Pyr-pHLIP</b>	52.2 ± 10.1	72.6 ± 3.3	-31.3 ± 1.7	0.25 ± 0.01

## FIGURES

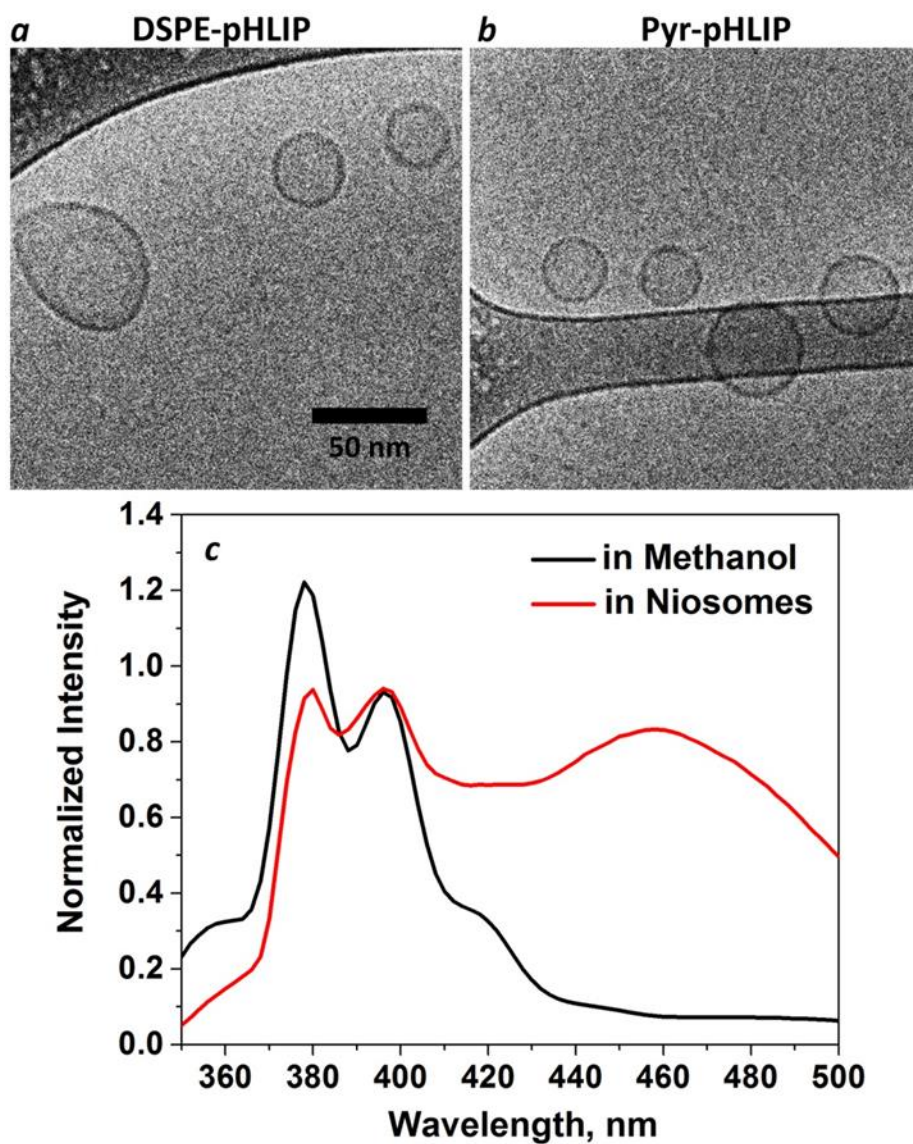


**Figure 1.** Cryogenic TEM image of the a) DSPE-pHLIP (5 mol%) and b) Pyr-pHLIP (5 mol%) coated Span20 (45 mol%) and cholesterol (50 mol%) niosomes. The images are obtained at 25,000x magnification. c) The fluorescence spectra of Pyr-pHLIP measured in methanol and Pyr-pHLIP incorporated in niosomes.

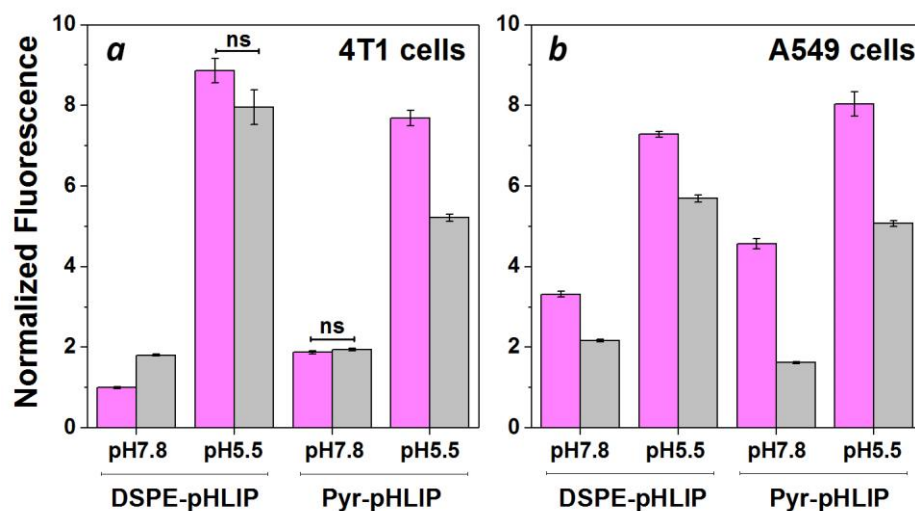


**Figure 2.** Normalized uptake of DSPE-pHLIP (5 mol%) and Pyr-pHLIP (5 mol%) coated Span20 (43 mol%) and cholesterol (50 mol%) niosomes containing 2 mol% of fluorescent R18 by 4T1 mammary (a) and A549 lung (b) cancer cells at pH 7.8 and pH 5.5 before (magenta columns) and after (gray columns) treatment with Trypan blue. The fluorescent signals were normalized by the rhodamine fluorescence intensity of 4T1 cells at pH 7.8 treated with DSPE-pHLIP before addition of Trypan blue. Statistically significant differences were determined by two-tailed unpaired Student's t-test, only statistically non-significant differences are indicated (ns means p-level > 0.05), all other differences in cellular uptake calculated at different pHs, as well as before and after Trypan Blue addition are statistically significant (p-level is less than 0.0001 in each case). The distribution of fluorescent signal in cells is presented in Figure S4.

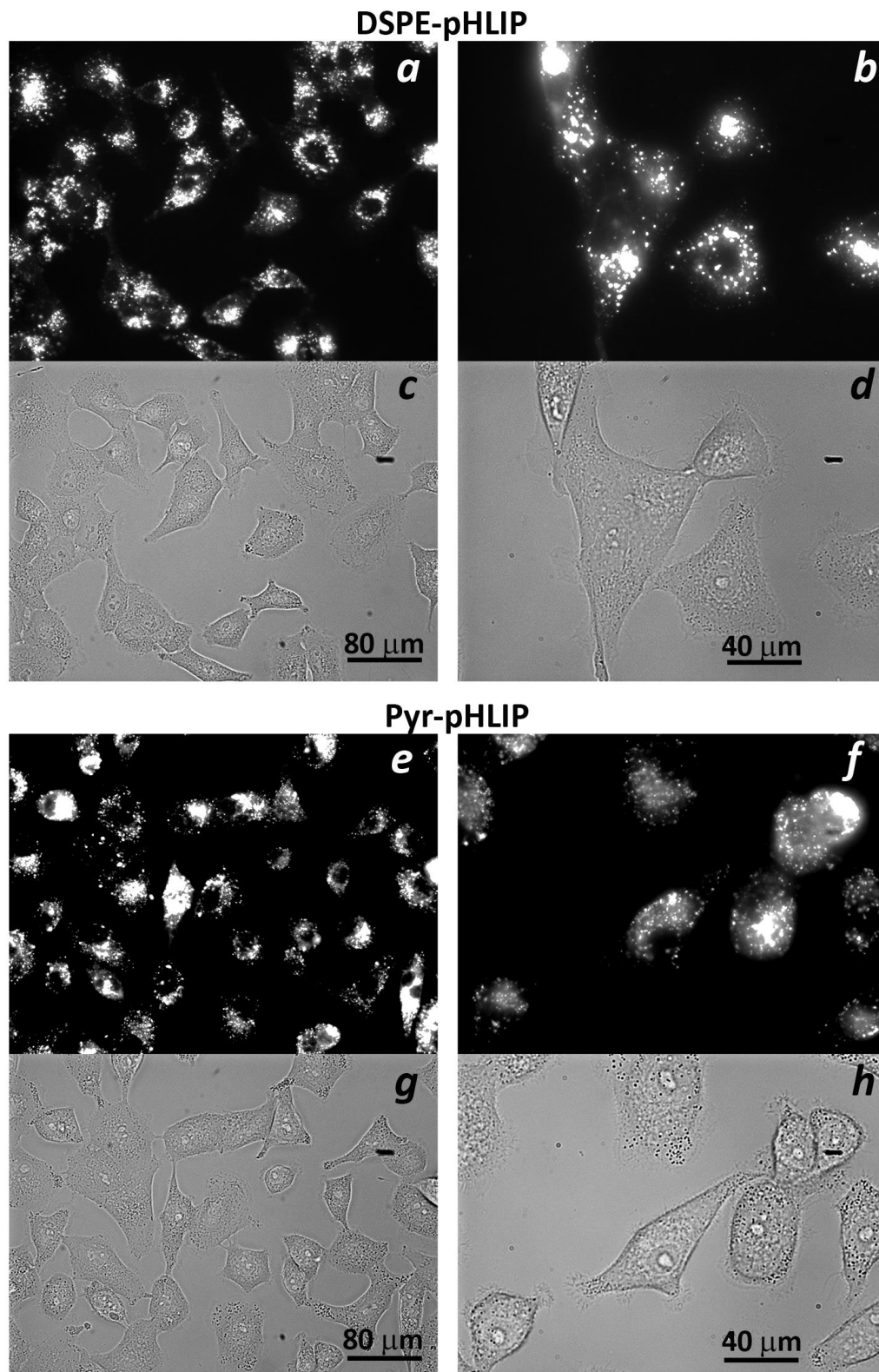


**Figure 3.** Uptake and cellular distribution of a-d) DSPE-pHLIP (5 mol%) and e-h) Pyr-

pHLIP (5 mol%) coated Span20 (43 mol%) and cholesterol (50 mol%) niosomes containing 2 mol% of fluorescent R18 by A549 lung cancer cells. Cells were treated with fluorescence niosomes at pH 6.4 for 1 hour, followed by washing, seeding cells in glass bottom collagen coated cell dishes and imaging at next day. Fluorescence (a, b, e, f) and phase contrast (c, d, g, h) images were obtained using 20x (a, c, e, g) and 40x (b, d, f, h) magnification objective lenses.

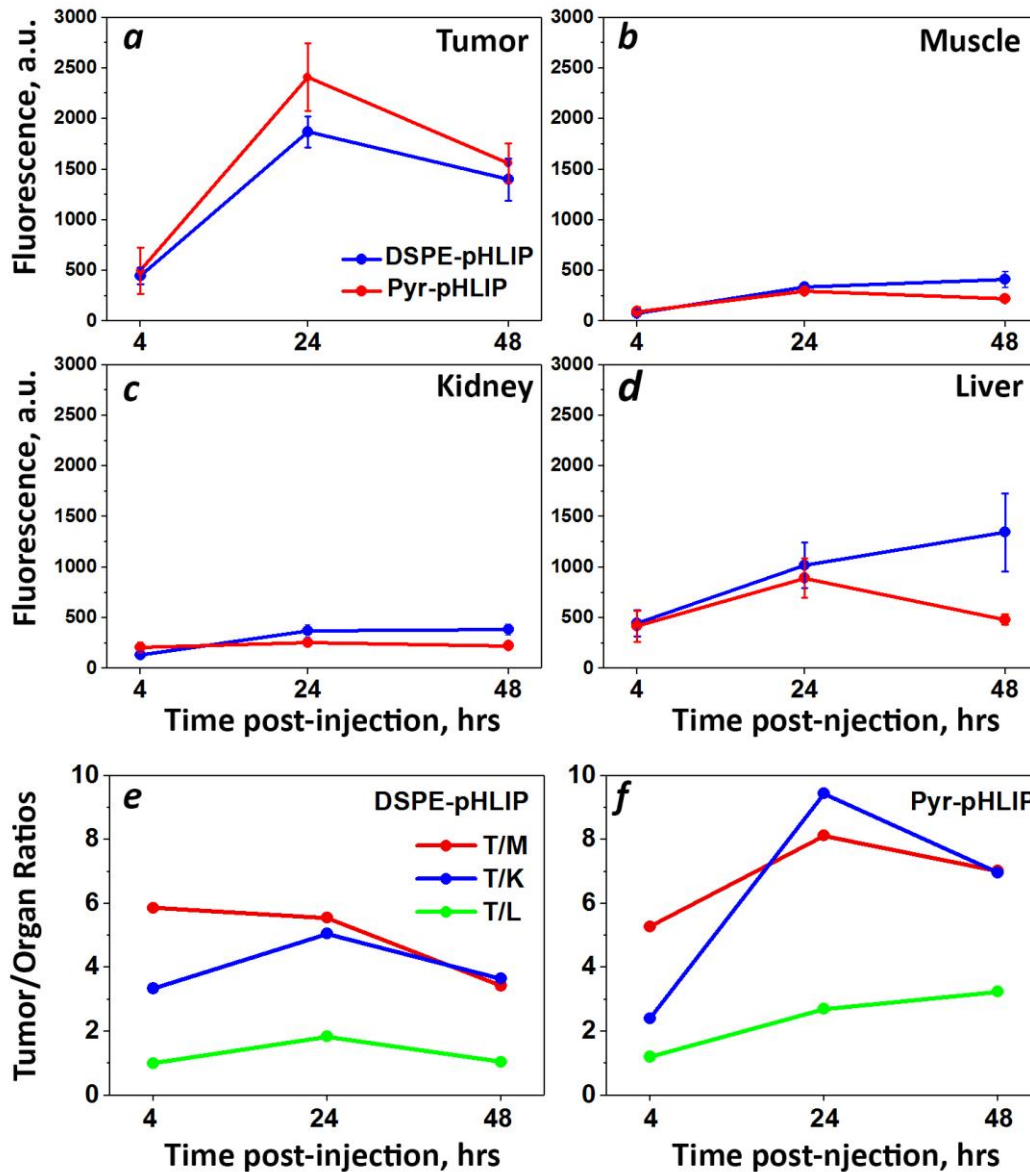


**Figure 4.** Time-dependent distribution of DSPE-pHLIP and Pyr-pHLIP (5 mol%), Span20 (43 mol%), cholesterol (50 mol%) and R18 (2 mol%) niosomes in a) tumor, b) muscle, c) kidney and d) liver at 4, 24 and 48 hours after single I.V. administration of the constructs. Tumor/Muscle (T/M), Tumor/Kidney (T/K) and Tumor/Liver (T/L) ratio calculated for DSPE-pHLIP (e) and Pyr-pHLIP (f) niosomes are shown. The values of mean surface fluorescence intensity of R18 in tissue and organs are presented in Table S1.

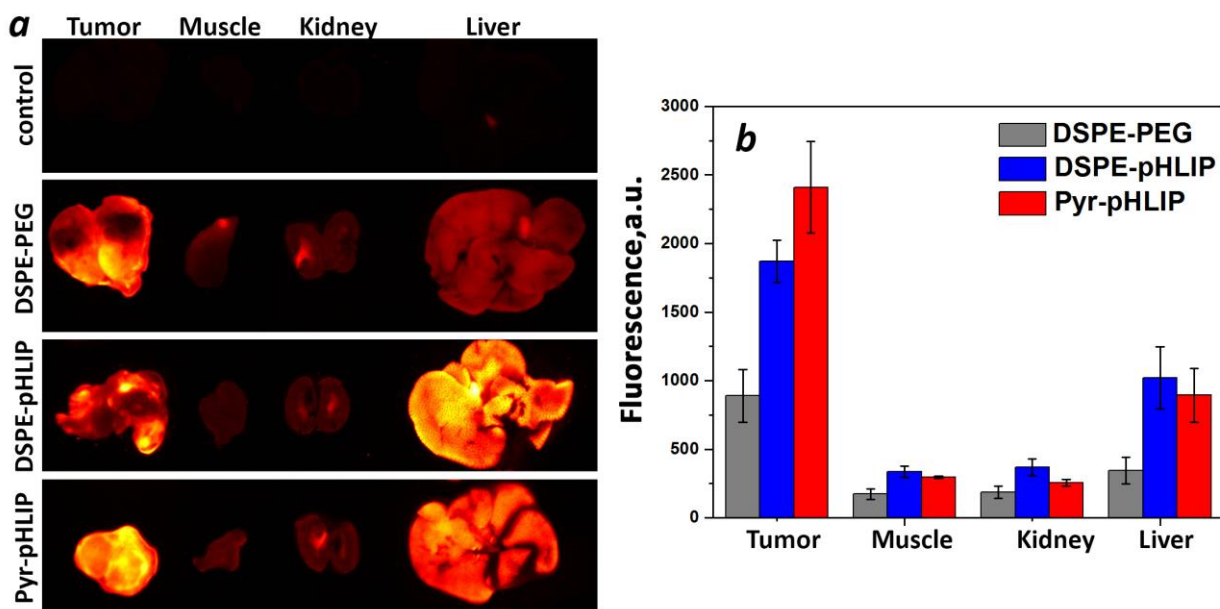


**Figure 5.** a) The representative rhodamine fluorescence images and b) mean surface fluorescence of tumor (cut in half), muscle, kidney (cut in half) and liver obtained by ex vivo imaging after collection of organs and tissues 24 hours after I.V. administration of pHLIP and PEG coated niosomes are shown (the autofluorescence signal is subtracted). The color coded fluorescent images shown on panel a are obtained at the same settings of the imaging instrument, the same exposure time (15 sec), and all of them were processed exactly the same way. Control means organs collected from the mouse with no injection of fluorescent niosomes, and it represents level of auto fluorescence signals in tissue. The values of mean surface fluorescence intensity of R18 in tissue and organs are presented in Table S2.

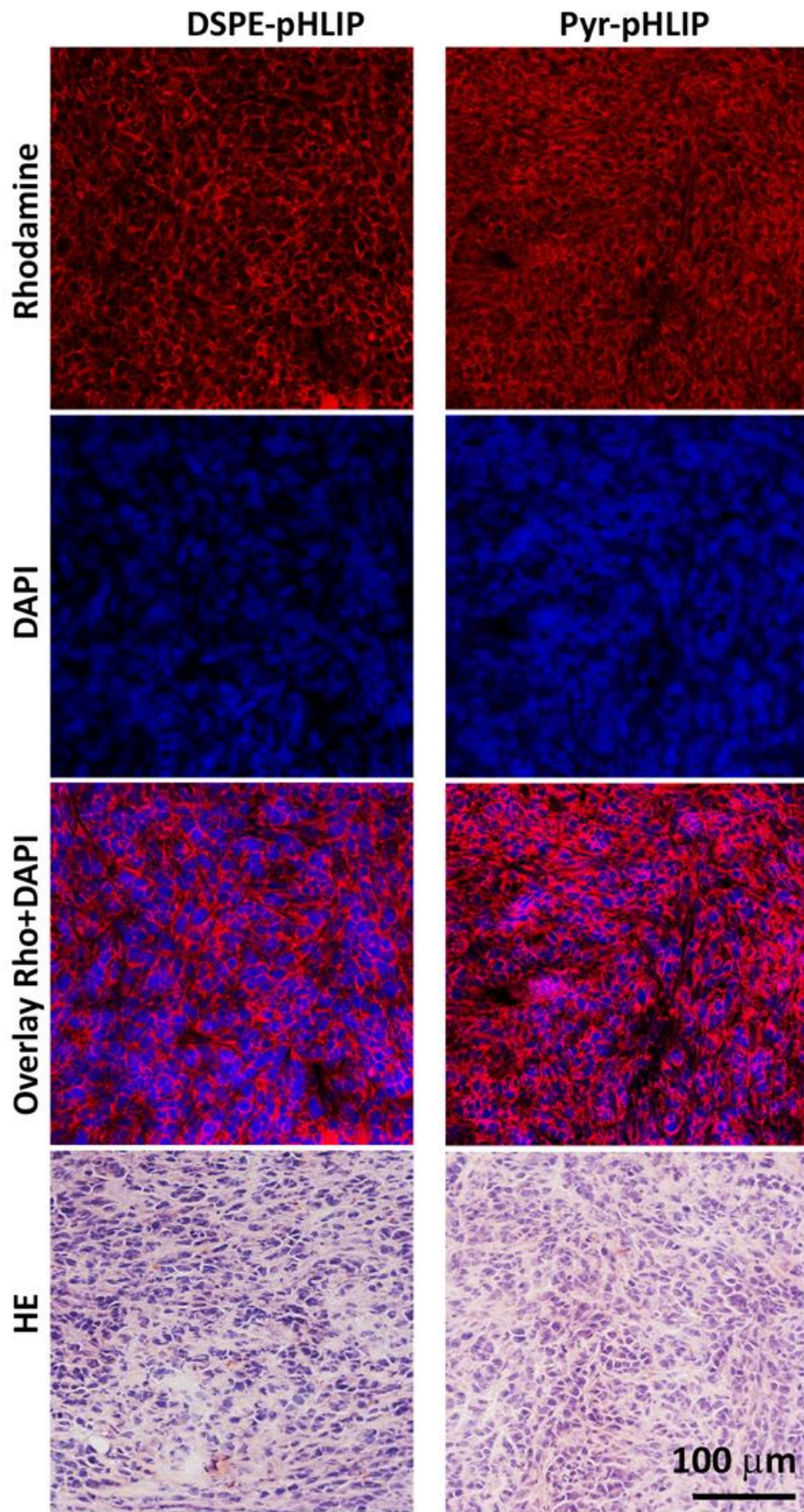


**Figure 6.** Distribution of R18 fluorescent signal in tumor sections obtained at 24 hours after I.V. injection of a-d) DSPE-pHLIP (5 mol%) and e-h) Pyr-pHLIP (5 mol%) coated Span20 (43 mol%), cholesterol (50 mol%) and R18 (2 mol%) niosomes. The rhodamine fluorescence (a, e), cell nucleus stained with DAPI (b, f), the overlay of rhodamine and DAPI fluorescence (c, g), and adjacent HE stained sections from the same tumor (d, h) are shown.

## **SUPPLEMENTARY INFORMATION**

### **pH-sensitive pHLIP® Coated Niosomes**

Mohan C. Pereira<sup>1</sup>, Monica Pianella<sup>2</sup>, Da Wei<sup>1</sup>, Anna Moshnikova<sup>1</sup>,  
Carlotta Marianecchi<sup>2</sup>, Maria Carafa<sup>2</sup>, Oleg A. Andreev<sup>1</sup>, Yana K. Reshetnyak<sup>1</sup>

<sup>1</sup>Physics Department, University of Rhode Island, 2 Lippitt Rd., Kingston, RI 02881,  
USA

<sup>2</sup>Dipartimento di Chimica e Tecnologie del Farmaco, Sapienza Università di Roma,  
P.zzle A. Moro 5 00185 Roma, Italia

**Table S1.** The mean and standard error values of the surface fluorescence intensity of R18 in tissue and organs at different time points after single I.V. administration of the DSPE-pHLIP or Pyr-pHLIP (5 mol%), Span20 (43 mol%), cholesterol (50 mol%) and R18 (2 mol%) niosomes. The autofluorescence signal, which was in the range of 200-250 was subtracted.

	<b>Time</b>	<b>DSPE-pHLIP n=3</b>	<b>Pyr-pHLIP n=3</b>
<b>Tumor</b>	4 h	447 ± 84	498 ± 232
	24 h	1870 ± 153	2409 ± 334
	48 h	1401 ± 209	1562 ± 194
<b>Muscle</b>	4 h	76 ± 34	94 ± 44
	24 h	337 ± 40	297 ± 7
	48 h	410 ± 80	223 ± 35
<b>Kidney</b>	4 h	134 ± 34	207 ± 55
	24 h	370 ± 60	255 ± 22
	48 h	384 ± 54	225 ± 20
<b>Liver</b>	4 h	446 ± 133	417 ± 154
	24 h	1020 ± 225	893 ± 195
	48 h	1343 ± 388	482 ± 52

**Table S2.** The mean and standard error values of the surface fluorescence intensity of R18 in tissue and organs at 24 hours after single I.V. administration of different formulations of niosomes: DSPE-PEG, DSPE-pHLIP or Pyr-pHLIP (5 mol%), Span20 (43 mol%), cholesterol (50 mol%) and R18 (2 mol%) niosomes.

	<b>DSPE-PEG n=4</b>	<b>DSPE-pHLIP n=3</b>	<b>Pyr-pHLIP n=3</b>
<b>Tumor</b>	889 ± 191	1870 ± 153	2409 ± 334
<b>Muscle</b>	173 ± 38	337 ± 40	297 ± 7
<b>Kidney</b>	187 ± 43	370 ± 60	255 ± 22
<b>Liver</b>	343 ± 97	1020 ± 225	893 ± 195

## Figures

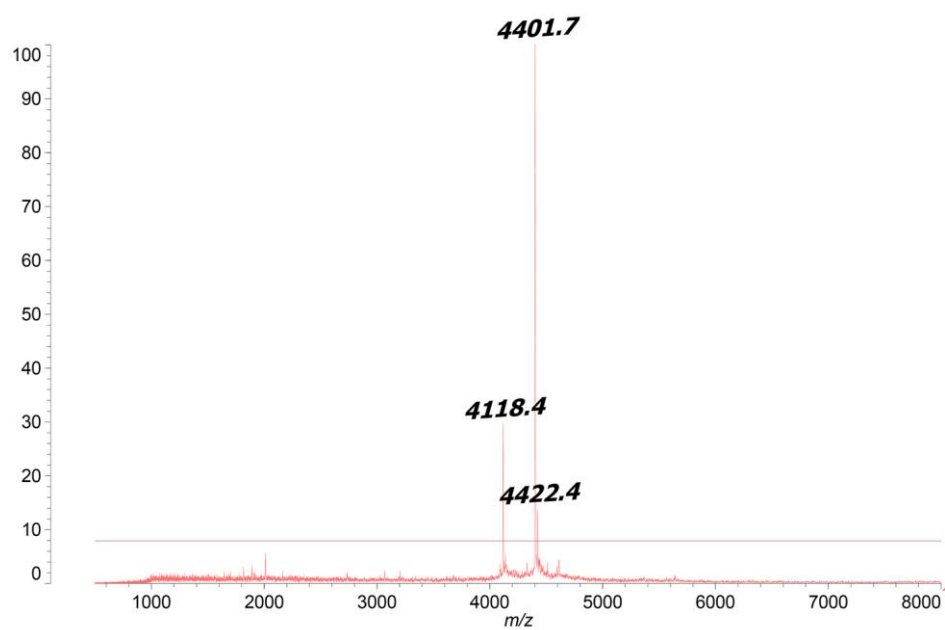


**Figure S1.** The SELDI-TOF mass spectrum of Pyr-pHLIP.

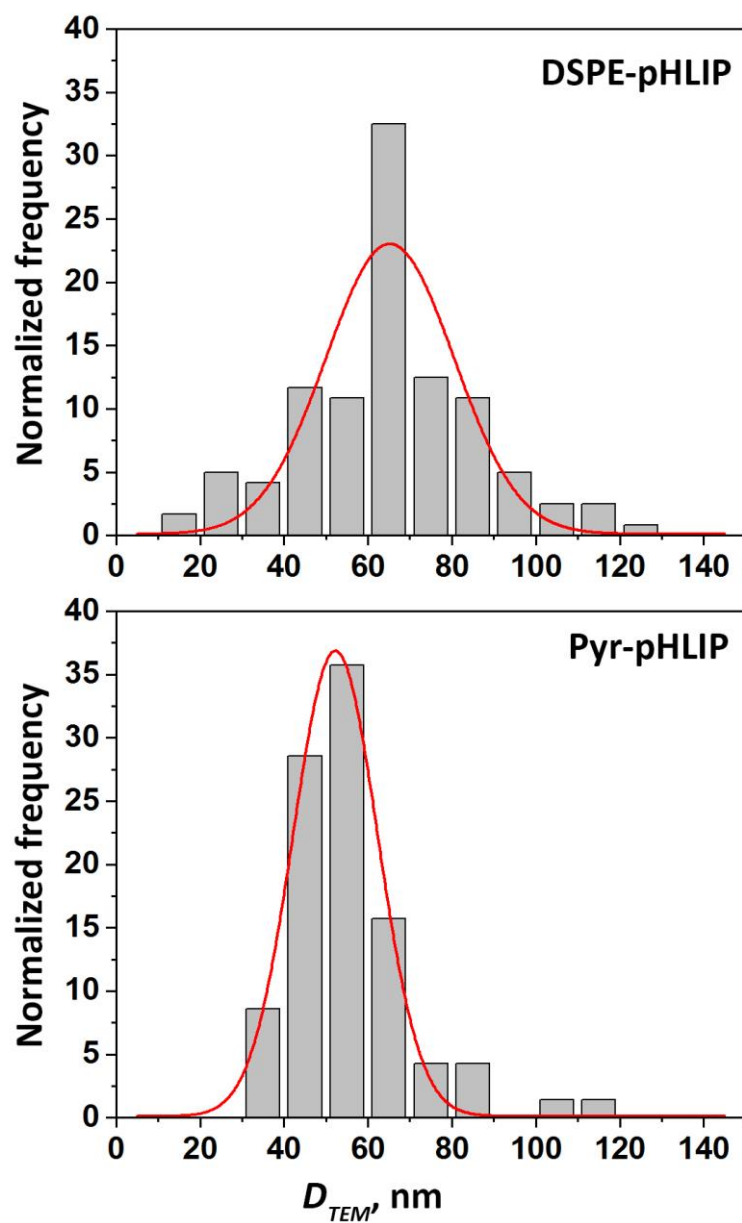


**Figure S2.** The size histograms of the DSPE-pHLIP and Pyr-pHLIP containing niosomes obtained after analyzing multiple cryo-TEM images.

The red lines demonstrate fittings by Gauss functions.

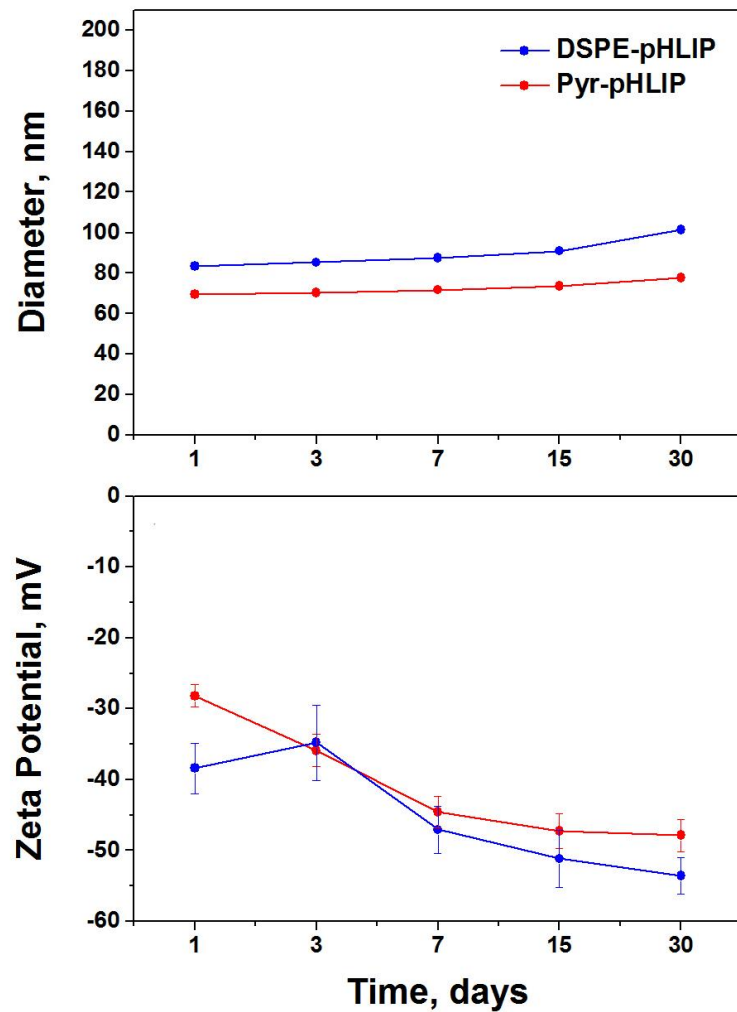


**Figure S3.** The results of stability study of DSPE-pHLIP and Pyr-pHLIP (5 mol%), Span20 (43 mol%), cholesterol (50 mol%) and R18 (2 mol%) niosomes in HEPES buffer in a course of 30 days (niosomes were kept refrigerated at 4°C). The changes of mean hydrodynamic diameter and Zeta potential are presented.

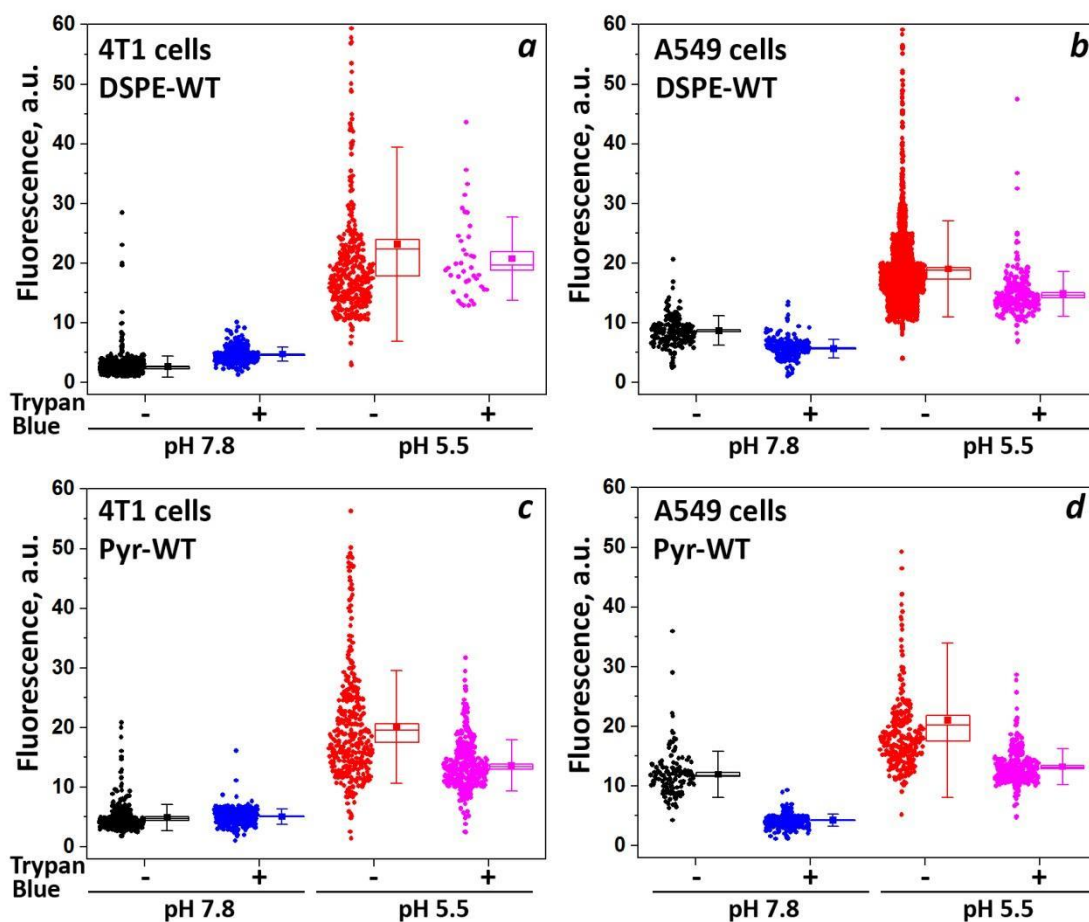


**Figure S4.** Fluorescent uptake of DSPE-pHLIP or Pyr-pHLIP (5 mol%), Span20 (43 mol%) and cholesterol (50 mol%) niosomes containing 2 mol% of fluorescent R18 by 4T1 mammary and A549 lung cancer cells at pH 7.8 and pH 5.5 before and after treatment with Trypan blue. The cellular uptake of fluorescent niosomes was assessed by counting of fluorescent cells using cellometer at 525 nm excitation and 595 nm emission channels.

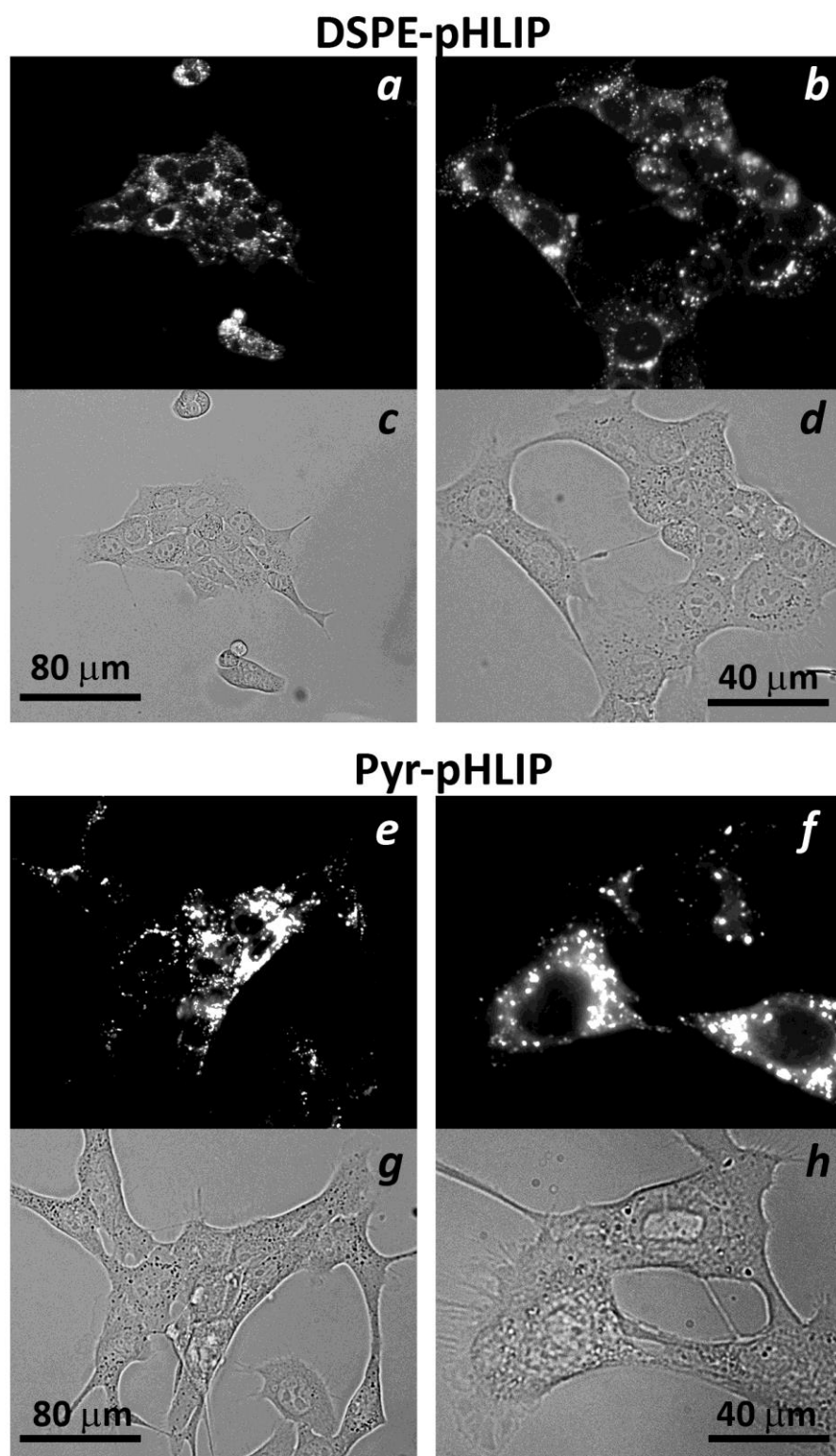


**Figure S5.** Uptake and cellular distribution of a-d) DSPE-pHLIP (5 mol%) and e-h) Pyr-pHLIP (5 mol%) coated Span20 (43 mol%) and cholesterol (50

mol%) niosomes containing 2 mol% of fluorescent R18 by 4T1 lung cancer cells. Cells were treated with fluorescence niosomes at pH 6.4 for 1 hour, followed by washing, seeding cells in glass bottom collagen coated cell dishes and imaging at next day. Fluorescence (a, b, e, f) and phase contrast (c, d, g, h) images were obtained using 20x (a, c, e, g) and 40x (b, d, f, h) magnification objective lenses.